

Rapid uplift in Laguna del Maule volcanic field of the Andean Southern Volcanic zone (Chile) 2007–2012

Kurt L. Feigl,¹ H el ene Le M evel,¹ S. Tabrez Ali,¹ Loreto C ordova,²
 Nathan L. Andersen,¹ Charles DeMets¹ and Bradley S. Singer¹

¹Department of Geoscience, University of Wisconsin-Madison, Madison, WI 53706, USA. E-mail: feigl@wisc.edu

²Observatorio Volcanol gico de los Andes del Sur (OVDAS), Servicio Nacional de Geolog a y Miner a (SERNAGEOMIN), Temuco, Chile

Accepted 2013 October 21. Received 2013 October 16; in original form 2013 January 1

SUMMARY

The Laguna del Maule (LdM) volcanic field in Chile is an exceptional example of postglacial rhyolitic volcanism in the Southern Volcanic Zone of the Andes. By interferometric analysis of synthetic aperture radar (SAR) images acquired between 2007 and 2012, we measure exceptionally rapid deformation. The maximum vertical velocity exceeds 280 mm yr⁻¹. Although the rate of deformation was negligible from 2003 January to 2004 February, it accelerated some time before 2007 January. Statistical testing rejects, with 95 per cent confidence, four hypotheses of artefacts caused by tropospheric gradients, ionospheric effects, orbital errors or topographic relief, respectively. The high rate of deformation is confirmed by daily estimates of position during several months in 2012, as measured by analysis of signals transmitted by the Global Positioning System (GPS) and received on the ground at three stations around the reservoir forming the LdM. The fastest-moving GPS station (MAU2) has a velocity vector of $[-180 \pm 4, 46 \pm 2, 280 \pm 4]$ mm yr⁻¹ for the northward, eastward and upward components, respectively, with respect to the stable interior of the South America Plate. The observed deformation cannot be explained by changes in the gravitational load caused by variations in the water level in the reservoir. For the most recent observation time interval, spanning 44 d in early 2012, the model that best fits the InSAR observations involves an inflating sill at a depth of 5.2 ± 0.3 km, with length 9.0 ± 0.3 km, width 5.3 ± 0.4 km, dip $20 \pm 3^\circ$ from horizontal and strike $14 \pm 5^\circ$ clockwise from north, assuming a rectangular dislocation in a half-space with uniform elastic properties. During this time interval, the estimated rate of tensile opening is 1.1 ± 0.04 m yr⁻¹, such that the rate of volume increase in the modelled sill is 51 ± 5 million m³ yr⁻¹ or 1.6 ± 0.2 m³ s⁻¹. From 2004 January to 2012 April the total increase in volume was at least 0.15 km³ over the 5.2-yr interval observed by InSAR. The inflating region includes most of the 16-km-by-14-km ring of rhyolitic domes and coulees. The similarity of high-silica rhyolite compositions on opposite sides of the ring and the concentration of rhyolitic eruptions since ~ 20 ka suggest that processes within a large silicic magma chamber are responsible for the current deformation.

Key words: Interferometry; Remote sensing of volcanoes; Volcano monitoring.

1 INTRODUCTION

The Southern Volcanic Zone of the Andes sits atop one of the most seismically and volcanically active subduction zones on Earth. The relative velocity of the Nazca Plate with respect to the South America Plate is 74 ± 2 mm yr⁻¹, as calculated from the MORVEL model (DeMets *et al.* 2010). As shown in Fig. 1, the relative motion is accommodated by mountain building punctuated by great earthquakes, including the M_w 9.5 event of 1960 and the M_w 8.8 event of 2010 February 27 (e.g. Lorito *et al.* 2011; Vigny *et al.* 2011). Lo-

cated 230 km east of the 2010 epicentre, Laguna del Maule (LdM) is a lake that sits in a 1-km-deep, 20-km-diameter basin on the crest of the Andes (Fig. 1). The associated LdM volcanic field extends over 500 km², forming part of the rear arc of the subduction zone (Hildreth *et al.* 2010).

The volcanic field at LdM has been mapped in detail by Wes Hildreth, Estanislao Godoy, Judy Fierstein and Brad Singer (Hildreth *et al.* 2010). The simplified geological map (Fig. 2) emphasizes the young rock units. The Quaternary suite of calc-alkaline igneous rocks includes compositions ranging from basalt to high-silica

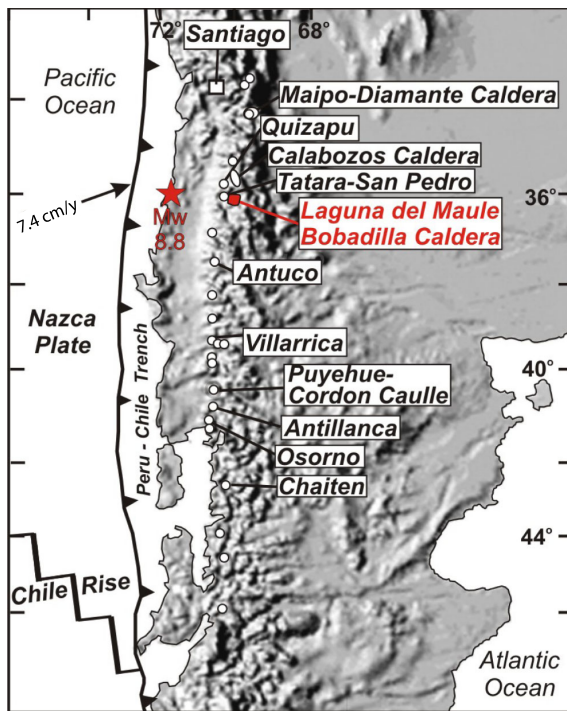


Figure 1. Map of the Southern Volcanic Zone (SVZ) of the Andes, showing the study area at Laguna del Maule (red rectangle), other major volcanoes (white circles), and the epicentre of the M_w 8.8 earthquake of the 2010 (red star, Lorito *et al.* 2011). The relative velocity (arrow) of the Nazca Plate with respect to the South America Plate is 74 ± 2 mm yr^{-1} (at 36°S , 72°W), as calculated from the MORVEL model (DeMets *et al.* 2010). Figure adapted from Singer *et al.* (2008).

rhyolite, as described by Hildreth *et al.* (2010). More than 350 km^3 of volcanic products have erupted from 130 identified vents in the last 1.5 Ma. Most of them are basaltic andesite or andesite, but isolated silicic eruptions have also occurred throughout the Quaternary. Welded ignimbrites indicate caldera-forming eruptions at 1.5 Ma, 950 ka and 336 ka. Of these, only the 950 ka Bobadilla caldera structure, located in the north side of the LdM basin, persists.

The volcanic field at LdM is noteworthy for its exceptional spatial and temporal concentration of rhyolitic volcanism during the Quaternary. Following the most recent glacial retreat at 25 ka, an unprecedented flare-up of silicic volcanism built a ring of 36 rhyodacite-and-rhyolite coulees and domes that encircle the lake (Singer *et al.* 2000). The most recent of these eruptions occurred ~ 2000 yr ago (Andersen *et al.* 2012). The postglacial eruptions became more evolved and voluminous with time, resulting in 6.4 km^3 of rhyolite compared to 1.0 km^3 of rhyodacite. Moreover, since the eruption of the Rhyolite of Loma de Los Espejos (unit ‘rle’ in Fig. 2) at 19 ka, andesitic volcanism has been of subordinate volume and isolated to the periphery of the LdM basin. The postglacial lavas display remarkably consistent major and trace element compositions (Hildreth *et al.* 2010; Andersen *et al.* 2012). Taken together, these observations suggest the presence of a shallow, caldera-sized, silicic magma body. In the conceptual model suggested by Hildreth *et al.* (2010), this magma body intercepts the ascent of mafic magma and serves as a common source for the postglacial silicic eruptions.

On shorter timescales, geodetic measurements indicate that the LdM volcanic field is actively deforming at exceptionally high rates. Using interferometric synthetic aperture radar (InSAR), Fournier *et al.* (2010) measured range change rates of more than 180 mm yr^{-1}

along the radar line of sight at 42° incidence between 2007 January and 2008 January in a round pattern centred on the west side of the lake named LdM. In this study, we analyse the time-dependent displacement field during the time interval from 2003 to 2012 using InSAR data. In addition, we use GPS data collected in 2012 to confirm the high rate of deformation. We then interpret the observed deformation field using elastic models of an inflating magma chamber.

2 INSAR OBSERVATIONS

2.1 Data selection

We have analysed synthetic aperture radar (SAR) data acquired by three satellite missions, as listed in Table 1. The ASAR sensor (e.g. McLeod *et al.* 1998) aboard the ENVISAT satellite mission operated by the European Space Agency (ESA) acquired two C-band SAR images. The resulting interferogram, spanning the time interval between 2003 March and 2004 February, ‘is coherent but shows no deformation’ (Fournier *et al.* 2010), a result that we quantify as the rate of change of the range $\partial\rho/\partial t = 0 \pm 10 \text{ mm yr}^{-1}$ along the radar line of sight at 23° incidence. Later, the PALSAR sensor (Rosenqvist *et al.* 2007) aboard the ALOS satellite mission operated by the Japanese Space Agency (JAXA) acquired L-band SAR images on eight distinct occasions (epochs) between 2007 February and 2010 April. More recently, the TanDEM-X (Krieger *et al.* 2007) and TerraSAR-X (Pitz & Miller 2010) missions operated by the German Space Agency (DLR) acquired X-band SAR images covering LdM on 10 epochs in 2011 and six epochs in 2012. Fig. 3 shows a map of radar reflectivity (‘backscatter’) calculated from the amplitude of the SAR image acquired by TerraSAR-X on 2012 March 14.

We combine the SAR images into interferometric combinations (interferograms). To generate the interferograms, we use the Diapason InSAR processing software (CNES 2006) developed by the French Space Agency, CNES (Massonnet & Rabaute 1993; Massonnet *et al.* 1993; Massonnet & Feigl 1998). The wrapped phase values are filtered using their 2-D spectra (Goldstein & Werner 1998). The wrapped phase values are then resampled using a quad-tree algorithm (Ali & Feigl 2012), thus reducing the number of data by two orders of magnitude, from $\sim 10^5$ to $\sim 10^3$. Although the quad-tree algorithm for compressing images (e.g. Samet 1984) has been applied previously to InSAR data (e.g. Jonsson *et al.* 2002; Simons *et al.* 2002), these studies perform unwrapping before resampling. In this paper, we do not unwrap the phase values at all. Instead, we use the General Inversion of Phase Technique (GIPhT) developed by Feigl & Thurber (2009).

The individual SAR images combine to form 12 useful pairwise interferograms, as listed in Table 1. In terms of graph theory (e.g. Harris *et al.* 2008), the epochs correspond to vertices on a graph; the pairs to edges. SAR images acquired using different radar frequencies cannot be combined to form interferograms unless their spectra overlap (e.g. Arnaud *et al.* 2003). Consequently, the graph for the LdM data set breaks into four separate trees, each of which is an acyclic and connected graph, as shown in Fig. 4. These trees are also known as ‘species’ (Feigl & Thurber 2009).

The observed values of wrapped phase change in early 2012 appear in the first panel (a) of Fig. 5. The principal signal in the interferograms is a concentric fringe pattern centred on the lake. The range from satellite to ground decreases with time, consistent with uplift. In this interferogram, one fringe of phase change corresponds to 15.5 mm of range change along the line of sight between the

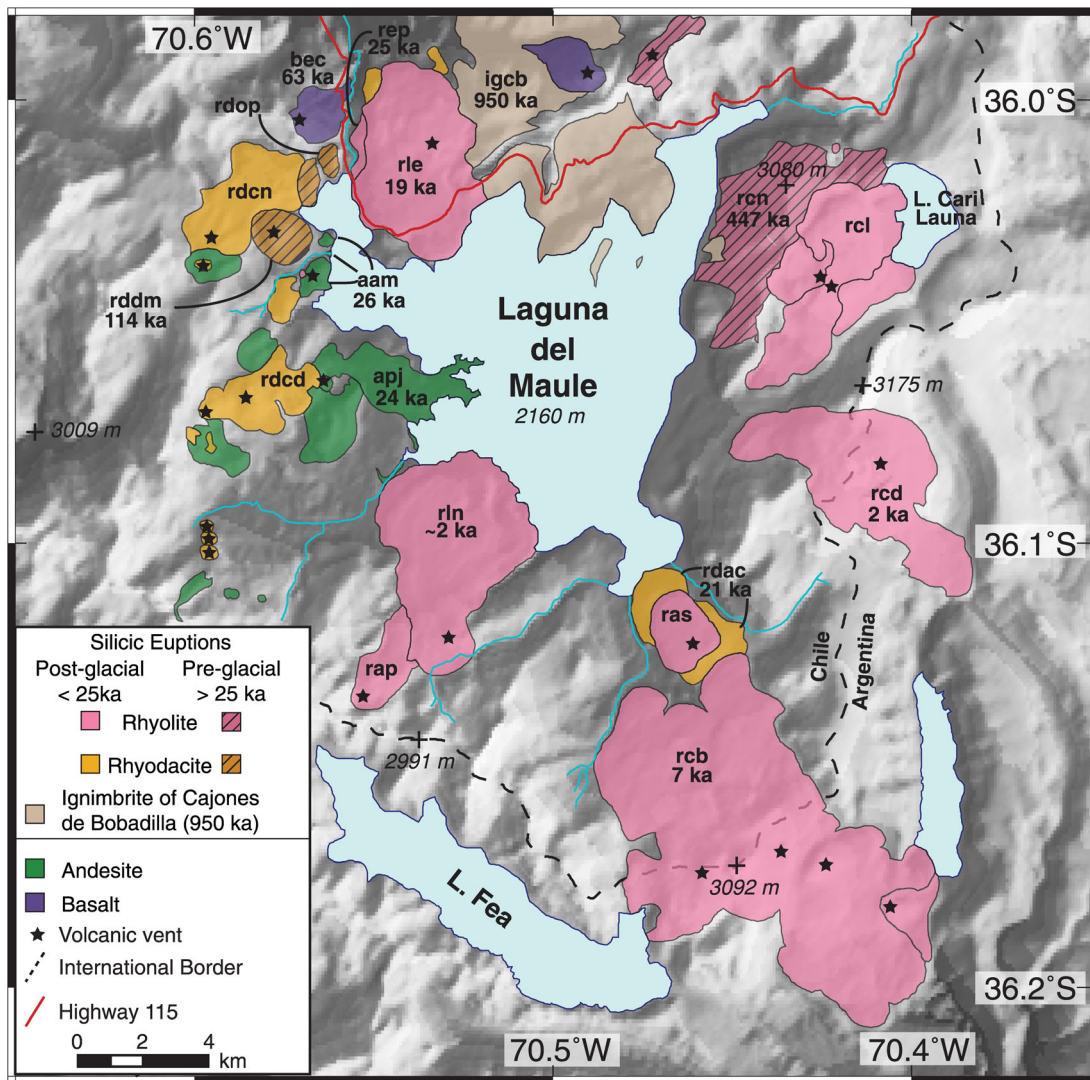


Figure 2. Simplified geological map highlighting the postglacial and silicic volcanism of the Laguna del Maule lake basin after Hildreth *et al.* (2010). The ages of selected units (Singer *et al.* 2000; Hildreth *et al.* 2010; Andersen *et al.* 2012) and field relationships demonstrate the basin-wide evolution during postglacial time. Unit names include: Rhyolite of Arroyo de Sepúlveda (ras), Rhyolite of Cerro Barrancas (rcb), Rhyolite of Colada Divisoria (rcd), Rhyolite of Cari Launa (rcl), Rhyolite of Loma de Los Espejos (rle), Rhyolite of Colada Las Nieblas (rln), Rhyodacite of Arroyo de la Calle (rdac), Rhyodacite of Colada Dendriforme (rdcd), Rhyodacite of the Northwest Coulee, Rhyolite of Cerro Negro (rcn), Rhyodacite of Domo del Maule (rddm), Rhyodacite west of Presa Laguna del Maule (rdop), Younger Andesite of West Peninsula (apj), Andesite of Arroyo Los Mellicos (aam), Basalt of El Candado (bec) and the Ignimbrite of Cajones de Bobadilla (igcb). The labels for some older or small units are omitted for simplicity.

satellite and the ground at an incidence angle of 35° from vertical. The two fringes indicate more than 31 mm of range change over the 44-d measurement interval between 2012 March 14 and April 27. If the motion were purely vertical, then the rate of uplift $\partial u_z / \partial t$ would be greater than 300 mm yr⁻¹.

2.2 Elimination of artefacts

Before interpreting the InSAR observations in terms of deformation on the ground, we consider, and then reject, four other possibilities. The first possibility is that errors in the orbital trajectories for the spacecraft are responsible for the observed fringe pattern. In this case, the artefacts would tend to form phase gradients mimicking topography. To quantify the probability of this possibility, we use these gradients to estimate adjustments to the orbital parameters

using the approach proposed by Kohlhase *et al.* (2003) and generalized by Bähr & Hanssen (2012). This approach (also known as ‘baseline adjustment’) is implemented in GIPhT (Feigl & Thurber 2009; Ali & Feigl 2012). It can estimate four parameters: the radial and along-track components of the spacecraft’s position and velocity vectors. Each of these four parameters is estimated at each of the acquisition epochs, except the first one in a tree, when the adjustment is set to zero as an arbitrary reference to regularize the solution (Feigl & Thurber 2009). The estimated values of the adjustments to the orbital parameters do not differ significantly from zero with 95 per cent confidence. We conclude that orbital errors are not responsible for the observed fringe pattern.

The second possibility is that perturbations in the troposphere contribute to the observed fringe pattern. For example, a plot of observed phase as a function of topographic elevation (Fig. 6) shows no obvious correlation between the two quantities. To quantify the

Table 1. List of interferometric pairs of SAR images, including dates of first and second image acquisitions, orbit numbers, altitude of ambiguity h_a , fringe spacing, track, frame, separation in azimuthal Doppler Δ_{Doppler} , perpendicular component of the ‘baseline’ vector between the two orbital trajectories at the times of acquisition, three components of the unit \hat{s} vector pointing from ground to satellite, and the name of the satellite mission.

Pair	1 st Epoch			2 nd Epoch			orbit1	orbit2	h_a metre	Δt days	1st epoch year	2nd epoch year	Trk	Fram	Δ_{Doppler} PRF	Bprrp metre	Fringe (mm)	δ_e dimless	δ_n dimless	δ_s dimless	Sat1	Sat2
	YYYY	MM	DD	YYYY	MM	DD																
P00	2004	FEB	03	2003	MAR	25	10084	5575	-147.16	-315	2004.0902	2003.2274	010	0000	+0.0964	49.6	28.1	0.3292	0.9402	0.7575	ENVI	ENVI
P01	2007	DEC	31	2010	JAN	05	10299	21035	-57.31	736	2007.9973	2010.0110	113	6450	+0.0050	1519.2	118.0	-0.6260	-0.1854	0.7575	ALOS	ALOS
P02	2008	FEB	15	2010	JAN	05	10970	21035	-57.74	690	2008.1229	2010.0110	113	6450	-0.0218	1454.5	118.0	-0.6260	-0.1853	0.7575	ALOS	ALOS
P03	2008	FEB	15	2010	APR	07	10970	22377	-239.66	782	2008.1229	2010.2630	113	6450	+0.0022	271.5	118.0	-0.6260	-0.1853	0.7575	ALOS	ALOS
P04	2008	APR	01	2010	APR	07	11641	22377	-76.00	736	2008.2486	2010.2630	113	6450	+0.0056	1155.5	118.0	-0.6266	-0.1854	0.7570	ALOS	ALOS
P05	2009	FEB	17	2007	FEB	12	16338	5602	72.58	-736	2009.1288	2007.1151	113	6450	+0.0047	-1170.8	118.0	-0.6234	-0.1849	0.7597	ALOS	ALOS
P06	2010	JAN	05	2007	FEB	12	21035	5602	-71.67	-1058	2010.0110	2007.1151	113	6450	+0.0270	1117.1	118.0	-0.6250	-0.1852	0.7583	ALOS	ALOS
P07	2010	FEB	20	2007	FEB	12	21706	5602	-55.40	-1104	2010.1370	2007.1151	113	6450	+0.0005	1506.2	118.0	-0.6253	-0.1852	0.7581	ALOS	ALOS
P08	2011	FEB	17	2011	MAY	05	3672	4841	103.36	77	2011.1288	2011.3397	28	0000	-0.0028	-109.0	15.5	-0.6447	-0.1697	0.7454	TDX1	TDX1
P09	2011	FEB	28	2011	APR	24	3839	4674	-114.84	55	2011.1589	2011.3096	28	0000	+0.0154	91.2	15.5	-0.6448	-0.1697	0.7453	TDX1	TDX1
P11	2011	FEB	28	2011	MAY	05	3839	4841	-796.31	66	2011.1589	2011.3397	28	0000	+0.0124	-15.3	15.5	-0.6448	-0.1697	0.7453	TDX1	TDX1
P12	2011	FEB	28	2011	MAY	16	3839	5008	188.33	77	2011.1589	2011.3699	28	0000	+0.0121	-34.2	15.5	-0.6448	-0.1697	0.7453	TDX1	TDX1
P13	2012	MAR	14	2012	APR	27	26330	26998	35.17	44	2012.1995	2012.3197	111	0000	-0.0062	-131.1	15.5	0.5014	-0.1227	0.8565	TSSX1	TSSX1

^apair analysed by Fournier *et al.* (2010).

magnitude of a possible tropospheric effect, we estimate the vertical component of the range change gradient $\partial(\Delta\rho)/\partial z$ in parts per million of topographic relief using GIPHT (Feigl & Thurber 2009). The estimated values do not differ significantly from zero with 95 per cent confidence at each of the acquisition epochs except the first. Even an extremely large tropospheric perturbation that altered the vertical component of the range gradient by $\sim 10^{-5}$ (Hanssen 2001) would contribute less than ~ 10 mm in range to the interferograms considered here because the topographic relief is less than ~ 1000 m in the part of the LdM basin covered by the interferograms. Neglecting turbulence, we infer that tropospheric effects are not responsible for the observed fringe pattern.

The third possibility is that heterogeneities in the distribution of electrons in the ionosphere contribute to the observed fringe pattern. Such effects have been invoked to explain closed fringes, such as the ~ 15 -km-long ‘kidney-shaped’ pattern observed in all of the interferograms involving the 56-mm-wavelength SAR image acquired on 1992 July 3, 3 d after the Landers earthquake (Massonnet *et al.* 1994; Massonnet & Feigl 1995). Nonetheless, it seems unlikely that such a phenomenon would recur repeatedly, in the same location, at three different radar wavelengths (31, 56 and 236 mm). Similarly, it seems unlikely that atmospheric effects would somehow conspire to produce the similarly shaped ‘bull’s eye’ pattern on 15 different epochs between 2007 and 2012, but not on the epochs forming the fringe-free interferogram spanning the time interval from 2003 to 2004. We conclude that atmospheric effects are not responsible for the observed fringe pattern.

The fourth possibility, that an error in the digital elevation model (DEM) creates an artefact in the InSAR results, can be excluded by two arguments: one qualitative and one quantitative. First, the shape of the observed fringe pattern does not resemble that of the topographic relief or that produced by interpolation of incorrect elevations (e.g. Massonnet & Feigl 1995). Second, the signal observed in the fringe patterns is much too large to be explained by an error in the DEM. Derived from the Shuttle Radar Topographic Mission, the DEM used to account for the topographic contribution to the interferograms has a (vertical) uncertainty of $\sigma_h \sim 20$ m in elevation (Falorni *et al.* 2005). For example, the interferometric pair shown in the first panel (a) of Fig. 7 has an orbital configuration such that the altitude of ambiguity h_a is ~ 72 m. The definition of h_a (Massonnet & Feigl 1998) implies that a hypothetical artefact in the DEM would have to be $5h_a \sim 360$ m in elevation to create the five-cycle concentric fringe pattern observed in Fig. 7(a). Such an artefact is extremely unlikely because it exceeds the DEM uncertainty by a factor of $5h_a/\sigma_h \sim (360\text{ m})/(20\text{ m}) \sim 18$. Furthermore, in the case of a hypothetical artefact in the DEM, the number of fringes would be inversely proportional to the altitude of ambiguity h_a in each pair (e.g. Massonnet & Feigl 1995). In fact, however, the number of fringes is roughly proportional to the time interval spanned by the interferometric pair.

2.3 Interpretation in terms of deformation

From the preceding four arguments, we conclude that the signal observed in the InSAR results is due to deformation on the ground.

Other InSAR observations indicate that rapid deformation began some time between 2004 February and 2007 February. We cannot resolve the exact date because no geodetic measurements were acquired around LdM during this time interval. The deformation between 2007 and 2010 was captured by the interferogram shown in Fig. 7. The five 118-mm fringes indicate more than 590 mm of range

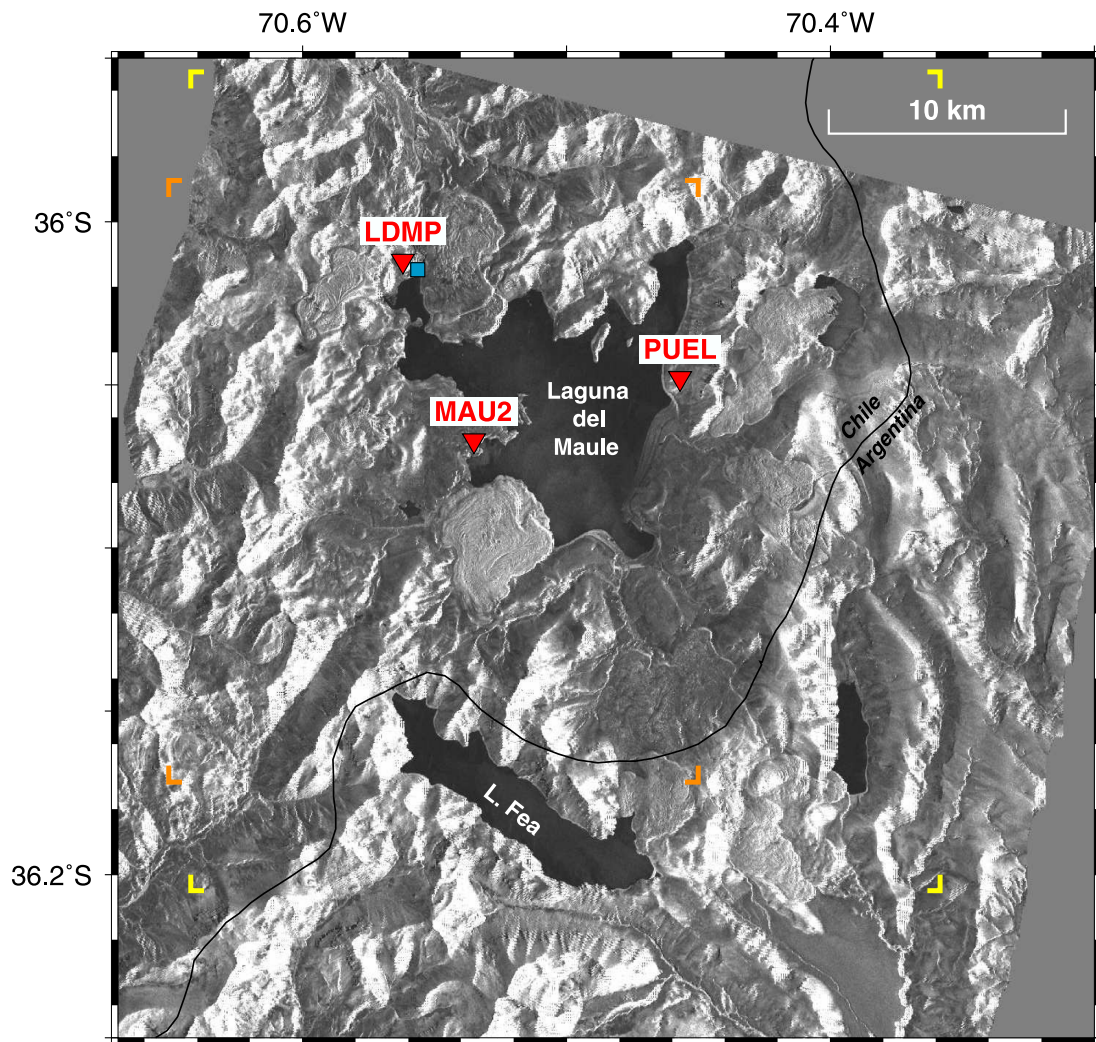


Figure 3. Map of study area at Laguna del Maule, showing the location of three GPS stations (red triangles), the dam (blue square), and the international border (black line) on a radar ‘amplitude’ image showing the reflectivity or ‘backscatter brightness’ as acquired on 2012 March 14 by the X-band SAR sensor aboard the TerraSAR-X satellite. Large rectangle implied by its corners marked in yellow delimits the subset of TerraSAR-X track 111 coverage that is analysed in subsequent figures. Small rectangle implied by its corners marked in orange delimits the subset of ALOS path 113 and TanDEM-X track 28 that is analysed in subsequent figures.

shortening at an incidence angle of 41° from vertical. If the motion were purely vertical, then the rate of uplift $\partial u_z / \partial t$ would be greater than 260 mm yr^{-1} . Similarly, Fig. 8 shows more than two concentric fringes of range decrease ($|\Delta\rho| > 31 \text{ mm}$) during a 77-d interval in early 2011. The corresponding rate of range shortening $-\partial\rho/\partial t$ is at least 147 mm yr^{-1} along the radar line of sight at 42° incidence. If the motion were purely vertical, then the rate of uplift $\partial u_z / \partial t$ would be greater than 200 mm yr^{-1} . The high rate of deformation in 2011 has been confirmed by a separate analysis of the InSAR data (Catherine Hickson, personal communication, 2011). The interferogram enlarged in Fig. 9 shows a rate of range shortening $-\partial\rho/\partial t$ of at least 300 mm yr^{-1} along the radar line of sight at 35° incidence during a 44-d interval in early 2012. Fig. 10 shows the range change in profile for the same time interval.

3 GPS MEASUREMENTS

In early 2012, the Southern Andes Volcanological Observatory (OV-DAS) of the Chilean SERNAGEOMIN agency began continuous

recording of GPS signals in the LdM study area at three permanent stations, named MAU2, PUEL and LDMP, as mapped in Fig. 3 and listed in Table 2. As of 2013 March, each of the three stations is equipped with a dual-frequency (L1 and L2) Trimble NetR9 receiver, a choke ring antenna, a hemispherical radome and solar panels. GPS data from the three stations (along with waveforms from broad-band seismometers at MAU2 and PUEL) are transmitted to OVDAS in real time for monitoring volcanic activity. Before 2012 March, however, the Trimble NetR9 GPS receiver at LDMP was not configured for telemetering.

At each of the three stations, the monument is a 38-mm-diameter steel rod inserted into a ~ 70 -cm-deep hole drilled into bedrock and encased in a concrete pillar. GPS station MAU2 is attached to a postglacial lava flow mapped as ‘younger andesite of West peninsula’ and abbreviated as unit ‘apj’ by Hildreth *et al.* (2010). It is located on the peninsula at the west side of the lake, within 1 km of the centre of the deformation pattern seen in the InSAR observations spanning 2007–2010. GPS station PUEL is anchored to the rhyolitic lava flow that emanated from Cerro Negro, mapped as unit ‘rcn’ by Hildreth *et al.* (2010). It is located on the east side of LdM.

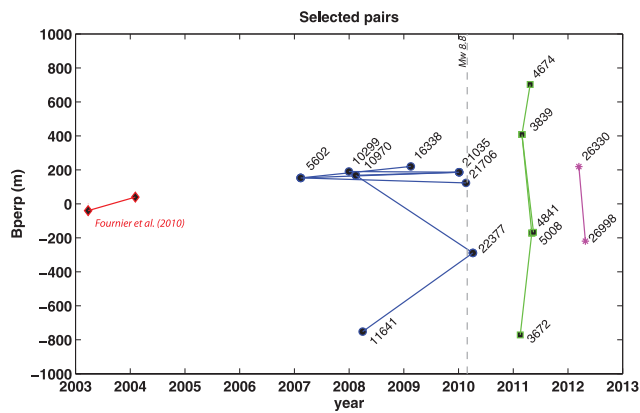


Figure 4. Orbital separation versus time for the radar images analysed in this study showing the individual images (epochs) as points with symbols. The interferometric pairs are shown as line segments connecting the points. The horizontal coordinate displays the acquisition date (epoch) of each image in decimal years. The labels next to the points give the corresponding orbit numbers. The vertical coordinate shows the orbital separation, or perpendicular component of the ‘baseline’ vector between the positions of the radar sensor at the acquisition epochs. The four ‘species’ (trees in the incidence graph) include: 2003–2004 (ENVISAT (Fournier *et al.* 2010), red diamonds), 2007–2010 (ALOS path 113, blue circles), 2011 January–April (TanDEM-X track 28, green squares) and 2012 January–April (TerraSAR-X track 111, magenta asterisks).

GPS station LDMP sits on top of a rhyodacitic dome mapped as unit ‘rdop’ by Hildreth *et al.* (2010). It overlooks the dam across the Rio Maule at the northwest corner of the lake.

The GPS data were analysed with the GIPSY software (release 6.1) from the Jet Propulsion Laboratory (JPL). Daily GPS station coordinates in a satellite-centric (non-fiducial) reference frame were estimated using a precise point-positioning strategy (Zumberge *et al.* 1997) and constrained by the latest IGS orbits available in mid-2012, *a priori* hydrostatic and wet tropospheric delays from Vienna Mapping Function (VMF1) parameters (<http://ggsatm.hg.tuwien.ac.at>), elevation- and azimuth-dependent GPS and satellite antenna phase centre corrections from IGS08 ANTEX files (available via ftp from sideshow.jpl.nasa.gov), and corrections for ocean tidal loading (<http://holt.oso.chalmers.se>). Wide- and narrow-lane phase ambiguities were resolved for all the data using GIPSY’s single-station ambiguity resolution feature. Seven-parameter Helmert transformations from JPL were used to transform the daily estimates of non-fiducial station location to IGS2008.

The station velocity at each site has been referred to the South America Plate by subtracting the predicted motion of the South America Plate. The angular velocity that best describes the motion of South America relative to IGS08 is determined from a weighted inversion of the velocities of 23 continuous GPS stations located in the stable interior of the South America Plate for which we also analyse daily data.

The resulting time series of relative position coordinates for MAU2, PUEL and LDMP appear in Figs 11–13, respectively. All three stations show rapid uplift rates that are an order of magnitude or more larger than their uncertainties. For example, station MAU2 moves upward at a rate of $280 \pm 4 \text{ mm yr}^{-1}$, as shown in Fig. 11. The horizontal components of velocity are also rapid and differ significantly from zero (with 95 per cent confidence) at all three stations, as listed in Table 2. For example, station MAU2 moves westward, away from the centre of the InSAR fringe pattern, at a rate of $180 \pm 4 \text{ mm yr}^{-1}$ with respect to South America, as shown in Fig. 11.

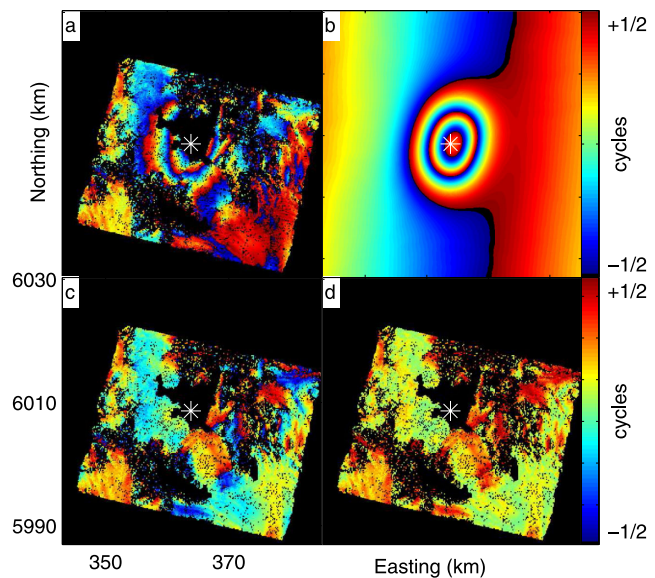


Figure 5. SAR interferograms for interferometric pair P12, spanning the 44-d time interval from 2012 March 14 to 2012 April 27 and showing the complete scene imaged by the TerraSAR-X satellite. The panels include (a) observed phase values; (b) modelled phase values calculated from the final estimate of the parameters in the Okada dislocation model; (c) final residual phase values formed by subtracting final modelled values from observed phase values and (d) angular deviations for final estimate. Asterisk indicates the location of the centroid of the modelled sill. One cycle of phase denotes 15.5 mm of range change. The TerraSAR-X orbit numbers are 26630 and 26998 in Strip 7 of Track 111. The altitude of ambiguity is 35.2 m. Unit vector $[E, N, U] = [-0.5082, -0.1277, 0.8517]$. The incidence angle is 35° from vertical. Coordinates are easting and northing in kilometre using the Universal Transverse Mercator (zone 19) projection (Snyder 1982).

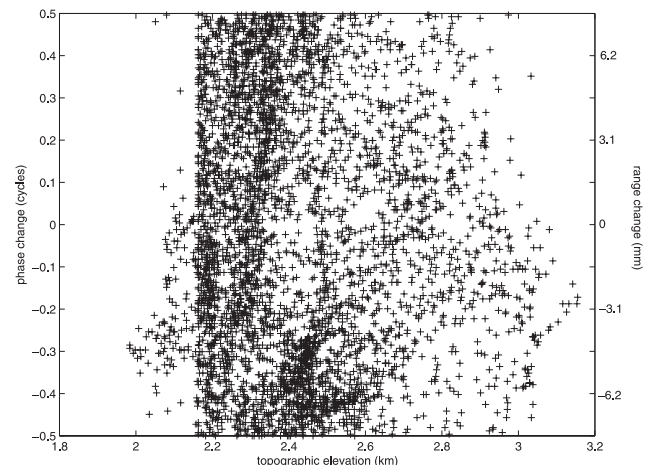


Figure 6. Observed, wrapped phase values in cycles as a function of topographic elevation for the interferogram spanning the time interval from 2012 Mar 14 to 2012 April 27 shown in the previous figure. One cycle of phase denotes 15.5 mm of range change.

4 MODELLING

In this section, we analyse the deformation on the ground by estimating the parameters in several different conceptual models, including gravitational loading and magmatic sources. To do so, we use GIPhT (Feigl & Thurber 2009) to estimate the optimal values of the parameters in a geophysical model by minimizing the circular mean deviation of the residual difference between the observed

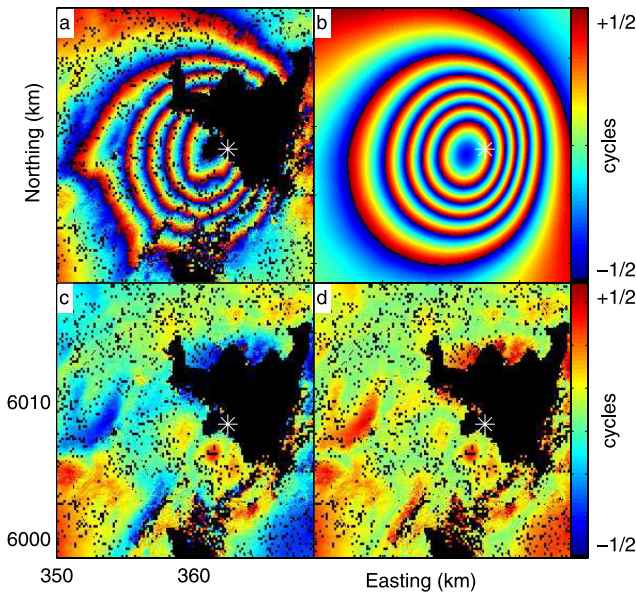


Figure 7. Interferograms for Laguna del Maule, spanning the 1058-d time interval from 2007 February 12 to 2010 January 5 (P06). The panels include (a) observed phase values; (b) modelled phase values calculated from the final estimate of the parameters in the Okada dislocation model; (c) final residual phase values formed by subtracting final modelled values from observed phase values and (d) angular deviations for final estimate. One cycle of phase denotes 118.1 mm of range change. The ALOS orbit numbers are 5602 and 21035. The altitude of ambiguity is 71.7 m. Unit vector $[E, N, U] = [-0.6242, -0.1851, 0.7590]$. The incidence angle is 41° from vertical. Coordinates are easting and northing in kilometre using the Universal Transverse Mercator (zone 19) projection (Snyder 1982).

and modelled values of wrapped phase. This objective function may be interpreted as the mean (or L1 norm) of the angular deviations between the observed and modelled values of wrapped phase. For each pixel in an interferogram, the angular deviation is defined by the ‘arc’ function that returns the lesser (in absolute value) of the two angles separating the direction of the observed phase from that of the modelled phase. The ‘arc’ function was originally defined by Mardia (1972), named by Niolaids & Pitas (1998), and expressed in eqs (14)–(16) of Feigl & Thurber (2009).

GIPhT then solves the non-linear inverse problem using simulated annealing, starting from an initial estimate of the parameters. A set of upper and lower bounds for each parameter constrains the search *a priori*. GIPhT offers several important advantages over previous strategies for analysing InSAR data. First, since GIPhT operates directly on ‘wrapped’ phase data ranging from $-1/2$ to $+1/2$ cycles, it avoids the possible pitfalls of unwrapping (Feigl & Thurber 2009). Secondly, GIPhT can evaluate the statistical uncertainty of the estimated model parameters because the residual phase values follow a von Mises distribution (Feigl & Thurber 2009).

The first conceptual model attributes the deformation to gravitational loading and unloading caused by changes in the level of water impounded in the reservoir behind the dam at LdM. The second model attributes the deformation to an inflating magma chamber at depth. Both models assume an elastic rheology with uniform material properties everywhere in a half-space. Poisson’s ratio is assumed to be $\nu = 1/4$.

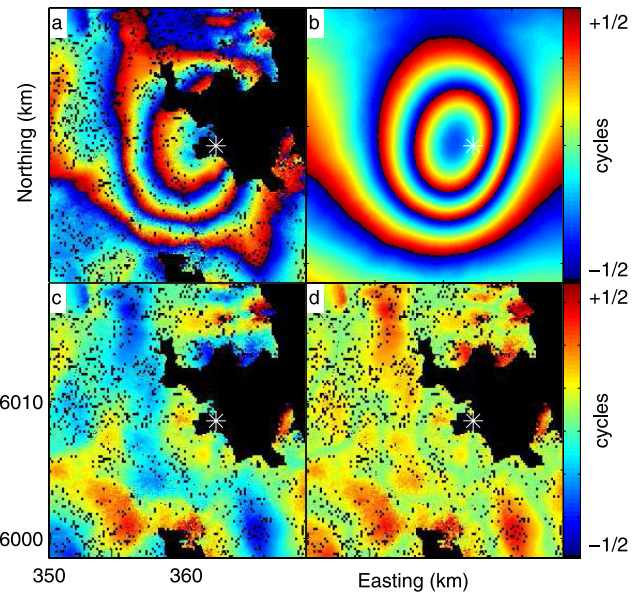


Figure 8. Interferograms for Laguna del Maule, spanning the 77-d time interval from 2011 February 17 to 2011 May 5 (P08). The panels include (a) observed phase values; (b) modelled phase values calculated from the final estimate of the parameters in the Okada dislocation model for an inflating sill; (c) final residual phase values formed by subtracting final modelled values from observed phase values and (d) angular deviations for final estimate. Asterisk indicates the location of centroid of the modelled sill. One cycle of phase denotes 15.5 mm of range change. The Tandem-X orbit numbers are 3672 and 4841 in Strip 12 of Track 28. The altitude of ambiguity is 103 m. Unit vector $[E, N, U] = -0.6418, -0.1718, +0.7475]$. The incidence angle is 42° from vertical. Coordinates are easting and northing in kilometre using the Universal Transverse Mercator (zone 19) projection (Snyder 1982).

4.1 Gravitational loading and unloading

The water level in the LdM varies by as much as $\Delta h \sim 10$ m over the course of a year, as shown in Fig. 14. Consequently, the incremental gravitational loading stress is $\rho_w \rho g \Delta h \sim 0.1$ MPa where ρ_w is the density of water and g is the gravitational acceleration. For example, we consider an interferogram spanning the 3-yr time interval from 2007 February 12 through 2010 January 5, as shown in Fig. 15. During this time interval, the water level dropped by 10.37 m, as recorded by the Ministry of Public Works in Chile. By assuming an elastic formulation (Pinel *et al.* 2007) and a water table that follows the shoreline, we calculate the modelled interferograms shown in Fig. 15. To do so, we consider four different values for the Young’s modulus E of the rock underlying the reservoir. The best-fitting estimate $E = 0.7$ GPa produces the modelled phase values shown in the last panel (d) of Fig. 15. The misfit of the gravitational loading model to the observed phase values, as evaluated by the circular mean deviation of the wrapped phase residuals, is 0.2134 cycles. This result is not significantly different (at the 95 per cent-confidence level) from the null model of no deformation or from models with Young’s modulus E ranging from 0.5 to 0.8 GPa. In Fig. 15, the previous panels (a–c) show values of 20, 10 and 5 G Pa, respectively for Young’s modulus E .

The best-fitting estimate of Young’s modulus E is 1–3 orders of magnitude lower than the conventional values of 4–210 GPa for crustal rocks derived from seismological studies and laboratory experiments of rock samples with P-wave velocities of 1.5 to 8.5 km s $^{-1}$ and densities of $\rho_d = 2.0$ to 3.5 Mg m $^{-3}$ (Brocher 2005), assuming Poisson’s ratio $\nu = 1/4$ and the relation $E = 5\rho_d V_p^2/6$. Similarly, our best-fitting estimate is much lower than the value of

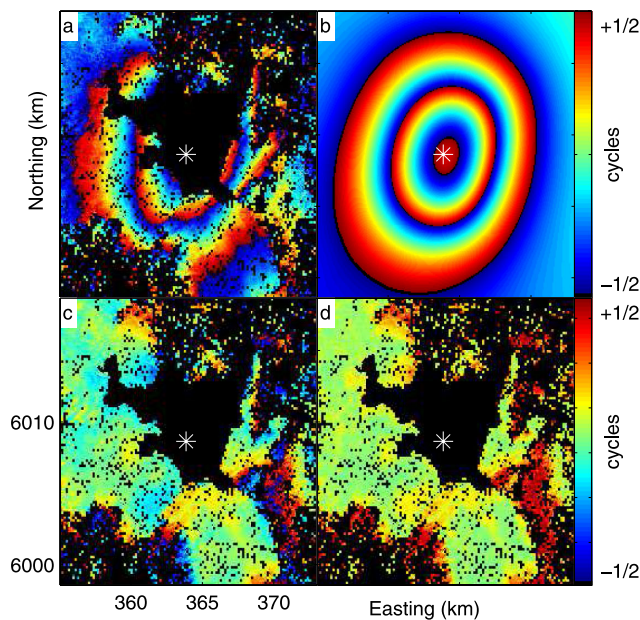


Figure 9. Enlarged SAR interferograms for pair P12, spanning the 44-d time interval from 2012 MAR 14 through 2012 APR 27 and showing only the subset from which data are drawn for estimating model parameters. The panels include (a) observed phase values; (b) modelled phase values calculated from the final estimate of the parameters in the Okada dislocation model; (c) final residual phase values formed by subtracting final modelled values from observed phase values; and (d) angular deviations for final estimate. Asterisk indicates the location of the centroid of the modelled sill. One cycle of phase denotes 15.5 mm of range change. The TerraSAR-X orbit numbers are 26630 and 26998 in Strip 7 of Track 111. The altitude of ambiguity is 35.2 m. Unit vector $[E, N, U] = [-0.5082, -0.1277, 0.8517]$. The incidence angle is 35° from vertical. Coordinates are easting and northing in kilometre using the Universal Transverse Mercator (zone 19) projection (Snyder 1982).

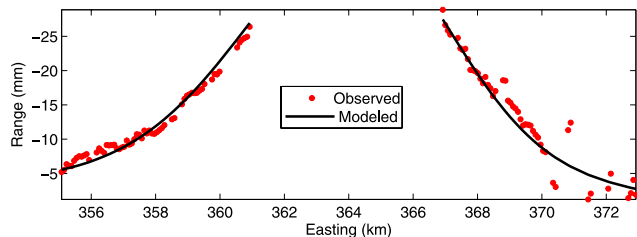


Figure 10. Range change along a profile striking due East, showing range change as observed (red dots) and modelled using the best-fitting parameters estimated for the sill model (black line) for interferometric pair P12, spanning the 44-d time interval from 2012 March 14 to 2012 April 27. The horizontal coordinate shows easting in kilometre. The profile is located at northing $Y_{UTM} = 6008.7$ km (latitude $S36.07^\circ$) using the Universal Transverse Mercator (zone 19) projection (Snyder 1982). On the vertical scale, 15.5 mm of range change corresponds to one cycle of phase.

$E = 44$ GPa (with $\nu = 0.31$) found by an InSAR-based study of the deformation attributed to the changing gravitational load of the Dead Sea (Nof *et al.* 2012).

During the 2-yr time interval from 2008 April 1 to 2010 April 7, the water level increased by 1.3 m (Fig. 14), thus increasing the gravitational load on the surrounding rock. Assuming the rock behaves as an elastic material, we would expect it to *subside* instantaneously. The observations from the corresponding interferogram (pair P04), however, show *uplift* of at least 600 mm along the radar line of sight at 41° incidence.

On the other hand, if the rock behaved as a viscoelastic medium, then the deformation would be more sensitive to the long-term trend in water level over timescales of the order of ~ 10 yr than to short-term (seasonal) variations on timescales of less than a year. Assuming a Maxwell viscoelastic rheology with viscosity $\eta \sim 40$ EPA.s and a Young's modulus $E \sim 70$ GPa, we would expect a relaxation time of $\tau \sim 2\eta/E \sim 36$ yr (Turcotte & Schubert 2002). Since the dam was constructed in 1958, we would expect the viscoelastic response to have begun by 2003. Yet interferometric pair P00, spanning the time interval between 2003 March 25 and 2004 February 3, shows no measurable deformation (Fournier *et al.* 2010).

Since the predictions of the elastic and the viscoelastic model are incompatible with the observed deformation, we reject the possibility that gravitational unloading could cause the observed deformation.

4.2 Magmatic sources

Alternatively, the second conceptual model interprets the observed deformation as the result of hydrothermal fluids and/or magma migrating within the crust. The centre of the source is located below the southwest part of the lake. The GPS stations move radially outward from it, consistent with the InSAR results from 2012 (Fig. 20).

In our preferred model, the source of the deformation is described as a rectangular prismatic sill, using a dislocation formulation with nine free parameters (Okada 1985). The estimated values of the model parameters are listed in Table 3. For InSAR data spanning from 2007 to 2010 (Fig. 7), the modelled sill increases in volume at a rate of $34 \pm 2 \times 10^6$ m³ yr⁻¹. It has a length of 7.6 ± 0.3 km, width of 5.5 ± 0.2 km and a dip of $22 \pm 2^\circ$ from horizontal.

To mitigate trade-offs between parameters, we constrain *a priori* the depth parameter to fall between 4.7 and 5.3 km in all the simulated annealing solutions. The validity of this constraint is discussed below.

Using the model of the rectangular sill, the estimated depth is 4.9 ± 0.1 km. The resulting modelled phase values shown in Fig. 7(b) reproduce the concentric pattern of the observed phase values shown in Fig. 7(a). Their differences, the wrapped residual phase values shown in Fig. 7(c), exhibit less than one fringe of unexplained signal. This model fits the resampled InSAR observations to within 0.1119 cycles in phase (13.2 mm in range), as measured by the circular mean deviation of the phase residuals, the objective function minimized by GIPhT. Considering the angular deviations of all the pixels in the 2.9-yr interferogram (Fig. 7d), we find their circular mean deviation to be 0.1440 cycles in phase (17.0 mm in range).

We also consider a source shaped like a prolate spheroid as parametrized by Yang *et al.* (1988) and implemented in Matlab by Fialko and Simons (Fialko & Simons 2000). The semi-major and semi-minor axes of the prolate spheroid are estimated to be $a = 3679 \pm 79$ m and $b = 875 \pm 12$ m, respectively. The rate of pressure increase is estimated to be $dP/dt = 155 \pm 3$ MPa yr⁻¹. The misfit for the best-fitting estimate of the parameters in the prolate-spheroid model is 0.1388 cycles in phase (16.4 mm in range) for the pixels sampled from the 3-yr interferogram shown in Fig. 7(a).

We also consider a model of a 'penny-shaped', pressurized crack with tapered edges, as parametrized by Sun (1969) and implemented in Matlab by Fialko *et al.* (2001). The rate of pressure increase is estimated to be $dP/dt = 1.2 \pm 0.02$ MPa yr⁻¹ on a horizontal sill with a radius of 4.7 ± 0.1 km. The misfit for the best-fitting estimate of the parameters in the penny-shaped crack model is 0.1303 cycles

Table 2. Position coordinates and estimated velocities for GPS stations near Laguna del Maule, with respect to the stable interior of the South America Plate, as defined by a network of 23 GPS stations.

Station	Latitude (deg)	Longitude (deg)	Height (m)	V_e (mm yr ⁻¹)	V_n (mm yr ⁻¹)	V_u (mm yr ⁻¹)
LDMP	-36.012435	289.437941	2391.48	-99.27 ± 47.96	84.72 ± 37.82	176.8 ± 81.3
MAU2	-36.067288	289.465393	2253.28	-180.07 ± 3.56	45.62 ± 2.17	279.8 ± 4.0
PUEL	-36.048310	289.543228	2417.52	9.24 ± 25.77	32.81 ± 20.44	86.4 ± 43.4
MAUL	-35.809636	289.178536	1183.92	-85.47 ± 10.13	39.25 ± 8.02	53.2 ± 16.9

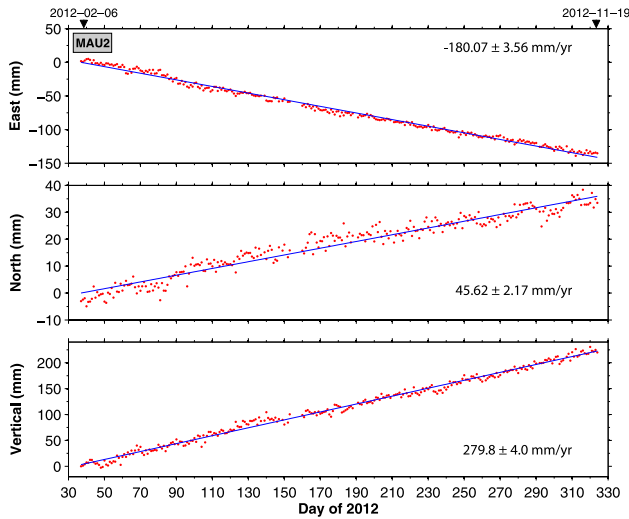


Figure 11. Time-series of relative position coordinates for GPS station MAU2 with respect to the stable interior of South America, showing relative displacement in the three directions: eastward (top), northward (middle) and upward (bottom). Labeled triangles indicate calendar dates of the first and last measurements, respectively. The blue lines indicate the best-fitting velocity as listed in Table 2.

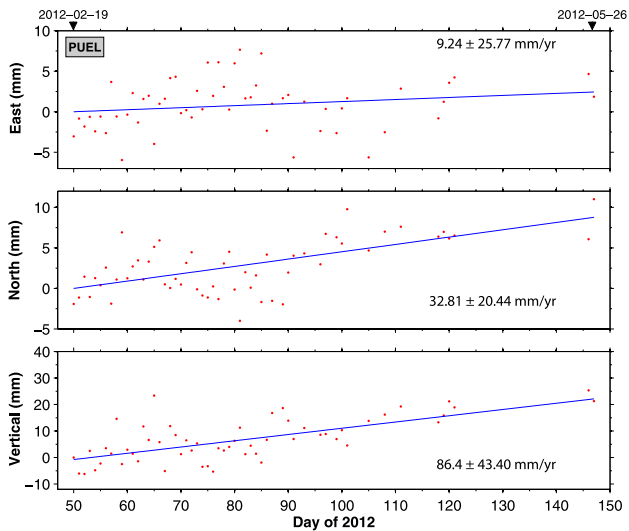


Figure 12. Time-series of relative position coordinates for GPS station PUEL with respect to the stable interior of South America. Plotting conventions as in previous figure.

in phase (15.4 mm in range) for the pixels sampled from the 3-yr interferogram shown in Fig. 7(a).

Finally, we also consider a spherical source (Mogi 1958; Segall 2010). The rate of volume increase is estimated to be $dV/dt = 36 \pm 0.6 \times 10^6 \text{ m}^3 \text{ yr}^{-1}$. The misfit for the best-fitting estimate of the parameters in the Mogi model is 0.1274 cycles in phase (15.0 mm

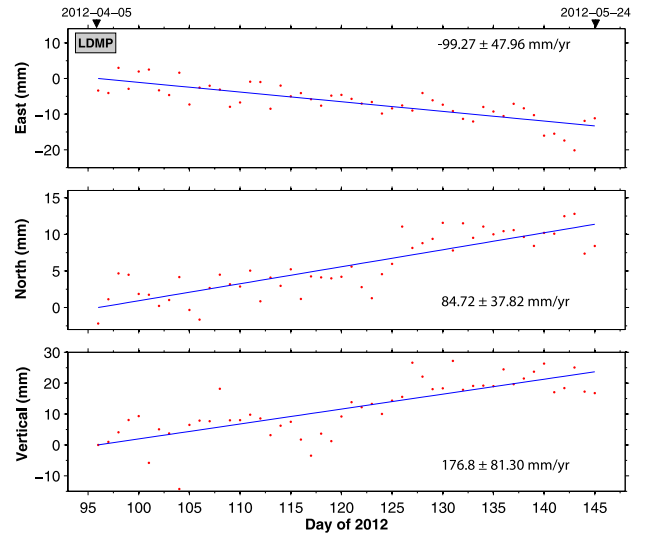


Figure 13. Time-series of relative position coordinates for GPS station LDMP with respect to the stable interior of South America. Plotting conventions as in previous figure.

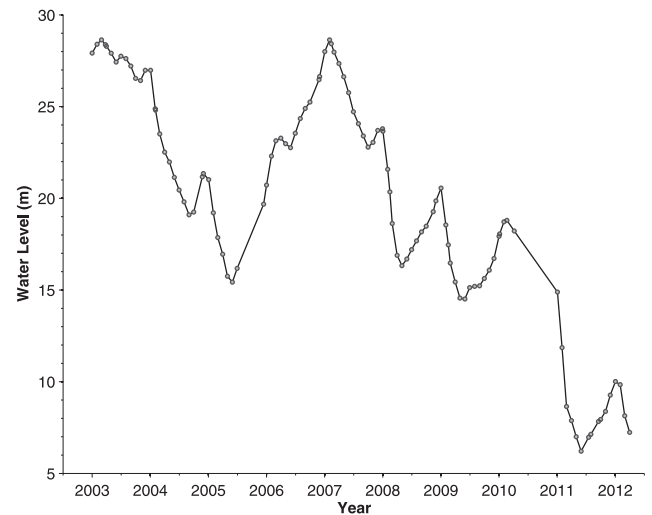


Figure 14. Water level in Laguna del Maule as a function of time, showing the value on the first day of each month, as extracted from daily measurements on the structure near the dam at Laguna del Maule by *El Ministerio de Obras Públicas, Dirección de Obras Hidráulicas* in Chile.

in range) for the pixels sampled from the 3-yr interferogram shown in Fig. 7(a).

4.3 Time dependence

Next, we apply the inverse modelling procedure to the 11 other interferometric pairs individually, as shown in Fig. 16. The estimated parameters and their uncertainties are listed in Table 3. The estimated

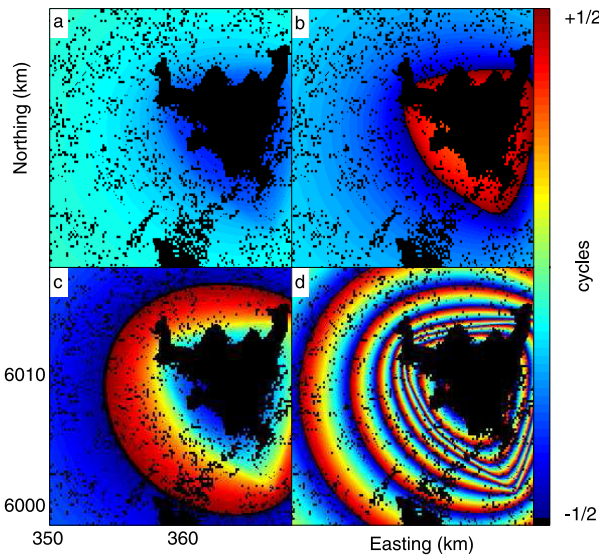


Figure 15. Interferograms for the 1058-d time from 2007 February 12 to 2010 January 5 (P06) showing modelled phase values calculated using various values of Young’s modulus E in an elastic formulation (Pinel & Jaupart 2000) to account for the change in gravitational load caused by the drop of 10.37 m in the lake level over the considered time interval. The panels include: (a) a low, but conventional value of Young’s modulus $E = 20$ GPa; (b) Young’s modulus $E = 10$ GPa; (c) Young’s modulus $E = 5$ GPa and (d) the value of Young’s modulus $E = 0.7$ GPa that best fits the data in Fig. 7a. One cycle of phase denotes 118.1 mm of range change. The ALOS orbit numbers are 5602 and 21035. Unit vector $[E, N, U] = [-0.6242, -0.1851, 0.7590]$.

depth of the modelled sill’s upper edge varies between 4.7 and 5.3 km below the free surface as a result of the constraint on this parameter. The typical uncertainties (70–280 m) on the depths estimated from each of the 12 pairs are consistent with their scatter, as measured by the standard error (40 m) of their weighted mean.

The rate of deformation is not constant in time, as shown in Fig. 17. While the interferometric pair spanning the interval from 2003 March to 2004 February ‘shows no deformation’ (Fournier *et al.* 2010), the rate of inflation in the modelled sill from 2007 to 2010 is $dV/dt = 31 \pm 1 \times 10^6 \text{ m}^3 \text{ yr}^{-1}$. To evaluate the time dependence, we perform a time-series analysis using temporal adjustment. This procedure converts the rate of volume change estimated over several time intervals into the integrated volume at each point in time or ‘epoch’ (Beauducel *et al.* 2000; Feigl *et al.* 2000; Schmidt & Burgmann 2003; Feigl & Thurber 2009; Grandin *et al.* 2009). We assume a piecewise linear parametrization, including four segments corresponding to the intervals beginning on the first epoch of each of the four trees in the incidence graph (Fig. 4). We estimate the rate of volume increase to be $0 \pm 5 \times 10^6$, $31 \pm 1 \times 10^6$, $29 \pm 2 \times 10^6$ and $51 \pm 8 \times 10^6 \text{ m}^3 \text{ yr}^{-1}$ for the four intervals, respectively (Fig. 18). The rate of inflation is significantly higher during the fourth interval (early 2012) than during the third interval (early 2011) with 95 per cent confidence. The location and intensity of the source driving the deformation appears to have changed sometime between mid-2011 and early 2012.

5 DISCUSSION

5.1 Geodetic comparisons

As in previous studies, the uncertainties of the parameter estimates are formal in the sense that they do not account for systematic

Table 3. Parameters in the elastic sill model, as estimated by GIPhT, including the final estimate and uncertainty for each of the 12 pairs.

ID	L (km)	W (km)	D (km)	Dip (deg)	Str (deg)	X (km)	Y (km)	U_3 (mm yr ⁻¹)	dV/dt [M(m ³ yr ⁻¹)]	t_1 (yr)	t_2 (yr)			
P01	7.52	0.34	4.96	0.16	0.07	4	365.06	0.15	6007.35	0.24	913	22	2007.9973	2010.0110
P02	7.73	0.33	5.24	0.25	0.13	3	364.97	0.16	6007.54	0.20	760	24	2008.1229	2010.0110
P03	7.69	0.31	4.72	0.22	0.13	3	364.95	0.13	6007.89	0.20	904	24	2008.1229	2010.2630
P04	7.67	0.33	5.42	0.35	0.08	2.5	365.12	0.26	6007.44	0.30	881	23	2008.2486	2010.2630
P05	8.36	0.52	6.37	0.15	0.07	2	365.71	0.20	6007.32	0.21	533	24	2007.1151	2009.1288
P06	7.86	0.26	5.22	0.09	0.11	1.5	364.96	0.09	6007.67	0.10	718	21	2007.1151	2010.0110
P07	7.65	0.33	4.88	0.15	0.11	1.9	364.97	0.09	6007.34	0.12	796	16	2007.1151	2010.1370
P08	9.03	0.99	4.72	0.37	0.12	4	364.38	0.32	6007.91	0.45	620	37	2011.1288	2011.3397
P09	7.03	0.65	6.04	0.92	0.16	8	365.58	0.79	6007.83	0.58	601	39	2011.1589	2011.3096
P10	8.97	0.22	6.13	0.18	0.11	4	366.08	0.24	6007.41	0.23	663	28	2011.1589	2011.3397
P11	6.41	0.14	6.20	0.10	0.20	4	365.23	0.24	6006.73	0.26	676	26	2011.1589	2011.3699
P12	9.00	0.29	5.33	0.38	0.28	5	366.30	0.27	6008.04	0.45	1072	48	2012.1995	2012.3197

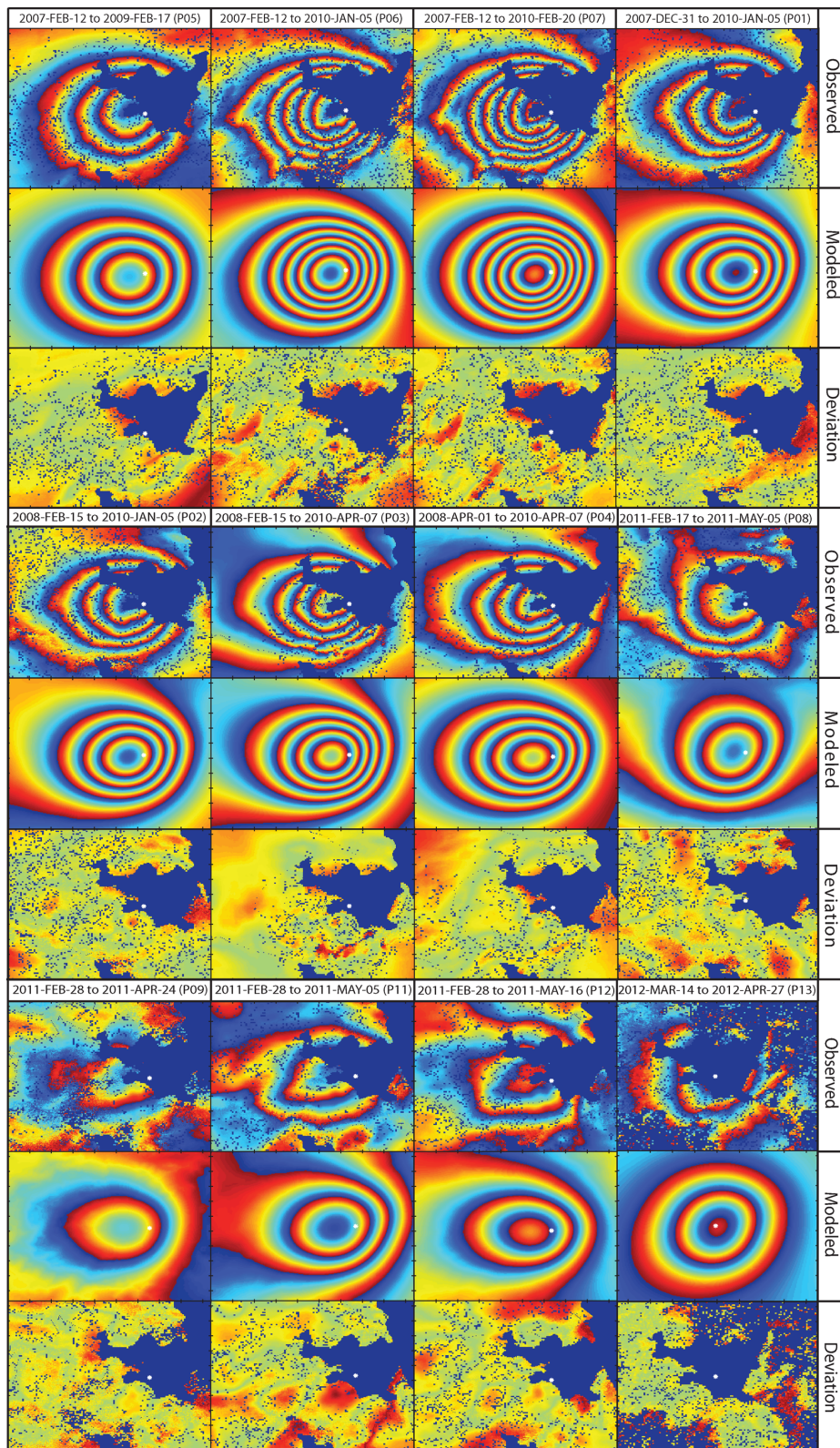


Figure 16. Interferograms for Laguna del Maule, for the 12 interferometric pairs, as numbered in Table 4. The panels include: (rows 1, 4 and 7) observed phase values; (rows 2, 5 and 8) modelled phase values calculated from the final estimate of the parameters in the Okada dislocation model; and (rows 3, 6 and 9), angular deviations for final estimate. Pairs labelled P01 through P07 are from the ALOS mission (118 mm of range change per fringe, or cycle of phase shift). Pairs labelled P08 through P12 are from the TanDEM-X mission (15.5 mm/fringe). Pair P13 is from the TerraSAR-X mission (15.5 mm/fringe). For each pair, the white asterisk indicates the projection of the centroid of the modelled sill. Tick marks are spaced every 5 km in Universal Transverse Mercator Easting and Northing.

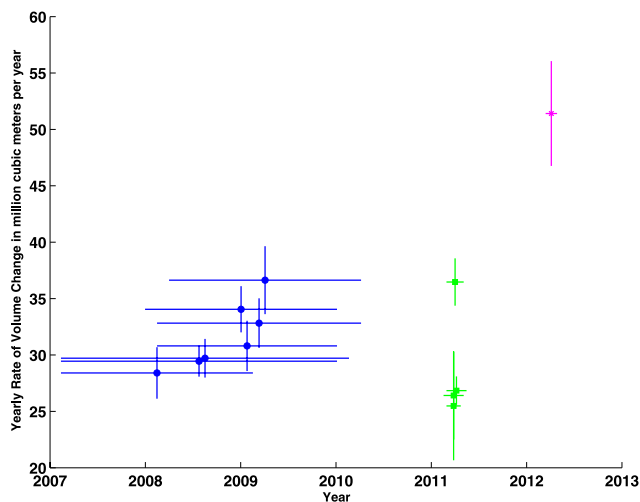


Figure 17. Values and uncertainties of model parameters as estimated from the InSAR data, showing the rate of volume change of the rectangular sill as a function of time. Coloured symbols represent the final estimates determined from each pair individually, using the same colour convention as in Fig. 4. Bars indicate the 1σ uncertainty as determined by GIPhT, assuming that the phase residuals sample a von Mises distribution (Feigl & Thurber 2009).

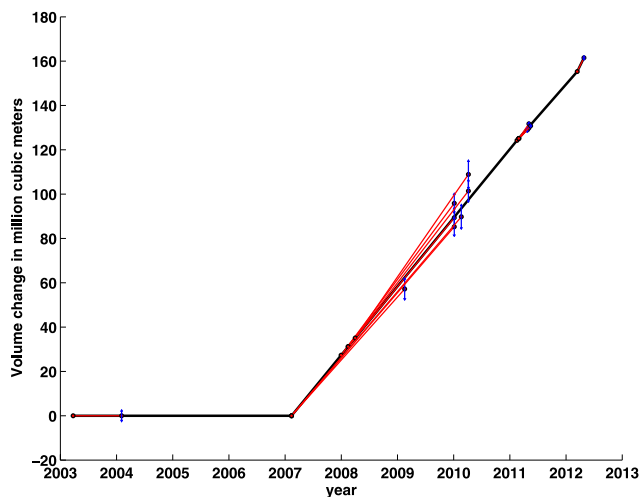


Figure 18. Volume change as a function of time as estimated from the individual pairs using temporal adjustment, assuming a piecewise linear model. Each red line segment represents an individual InSAR pair connecting the first epoch (red dot) taken as a reference and plotted arbitrarily on the modelled curve (black) with the second epoch (blue dot with bar denoting $\pm 1\sigma$). The slope of each red line segment denotes the rate of volume change estimated from the corresponding InSAR pair. The modelled curve (black) assumes a piecewise linear model with four free parameters corresponding to the rate of volume change over the four time intervals measured by InSAR: 2003–2004 (Fournier *et al.* 2010), 2007–2010 (ALOS), 2011 January–April 2011 (TanDEM-X) and 2012 January–April (TerraSAR-X). During the gaps between the measured time intervals, the rate of change is (arbitrarily) assumed to continue at the same rate as in the preceding interval.

errors in the measurements, correlations in the resampled data set, or oversimplifications in the physical earth model. For example, we assume the values of the wrapped phase values, as determined by the quad-tree resampling procedure, to be independent in all our statistical tests. Although neighbouring pixels are correlated in space (Hanssen 2001; Lohman & Simons 2005) and pairs sharing a common epoch are correlated in time (Biggs *et al.* 2007), the parameter

Table 4. List of parameters in the affine transformation estimated to adjust InSAR model to GPS velocities.

Parameter	Value	Unc ^a	Dimensions
V_e	-53.74	± 13.97	[mm yr ⁻¹]
V_n	24.90	± 12.30	[mm yr ⁻¹]
V_u	-2.85	± 17.82	[mm yr ⁻¹]
dV_e/dX	-1.36	± 4.09	[1E-6/yr]
dV_e/dY	-2.99	± 4.05	[1E-6/yr]
dV_n/dX	-1.91	± 3.58	[1E-6/yr]
dV_n/dY	-1.44	± 3.52	[1E-6/yr]
dV_u/dX	2.24	± 5.19	[1E-6/yr]
dV_u/dY	5.59	± 5.07	[1E-6/yr]

^aUncertainty is 1 standard deviation, after scaling by Mean Standard Error.

estimates are robust to different (randomly selected) subsets of the pixels, as discussed previously (Feigl & Thurber 2009; Ali & Feigl 2012).

The GPS and InSAR measurements indicate exceptionally high rates of deformation from 2007 January to 2012 May. Before comparing the InSAR results to the GPS velocity, we adjust the modelled velocity field calculated from the parameters estimated from the 2012 InSAR data using an affine transformation. The adjustment uses a standard weighted least-squares algorithm to estimate nine additional parameters, including three components of a translational velocity vector and $6 = 3 \times 2$ components of the deformation gradient tensor, that is, the partial derivatives of the three components of the vector velocity field with respect to the two horizontal coordinates. To estimate the nine parameters in the affine transformation, we consider 12 data, including the three-component velocity vectors at the three GPS stations MAU2, PUEL and LDMP in the LdM study area, as well as a fourth station, MAUL, that is located some ~ 35 km NW of LdM. The resulting estimates of the nine affine parameters and their uncertainties appear in Table 4.

The affine transformation may be interpreted as deformation that is not explained by the model describing the inflating sill below the LdM volcanic field. For example, some of the observed motion may be due to transient post-seismic deformation following the M_w 8.8 earthquake of 2010 February 27 (e.g. Lorito *et al.* 2011; Vigny *et al.* 2011). The estimated translational velocity of the LdM study area with respect to South America in 2012 is approximately 59 mm yr^{-1} at an azimuth of $N65^\circ W$. Since none of the components of the deformation rate tensor are significantly different from zero with 95 per cent confidence, we neglect the effect of transient phenomena, such as post-seismic relaxation, at spatial scales longer than the ~ 20 km width of the LdM study area.

We then apply the nine-parameter affine transformation to the InSAR modelled velocity field. As shown in Fig. 19, the vertical components of the GPS velocity vectors agree (to within their uncertainties) with those calculated using the sill-model parameters estimated from the interferogram spanning 2012 January to March (Fig. 9) and the affine transformation at GPS stations MAU2 and PUEL. At station LDMP, the two estimates of the uplift disagree by more than 100 mm yr^{-1} , but the discrepancy is not significantly different from zero with 95 per cent confidence. The large uncertainty in the GPS measurement of the vertical velocity at LDMP is a consequence of the short duration of the time series. Since the GPS station at LDMP did not yet include telemetering, only 50 d of data were retrieved before snowfall in late 2012 May.

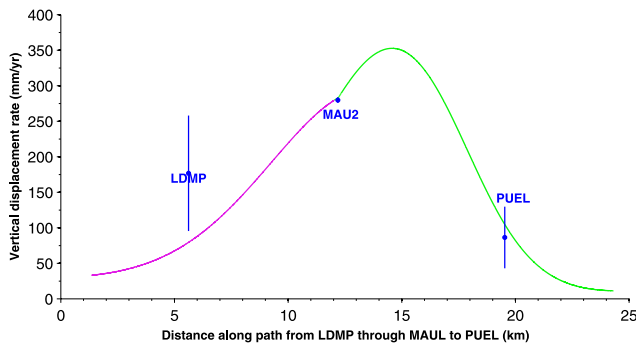


Figure 19. Vertical displacement rate $v_z = dz/dt$ on a path from GPS station LDMP through MAU2 to PUEL. The three circles denote the rate of vertical uplift with respect to South America, as measured by GPS at the three stations, LDMP, PUEL and MAU2. The curves show the modelled values of vertical displacement rate calculated from the final estimate using the InSAR data for 2012 January–April from TerraSAR-X, after the affine transformation described by the parameters listed in Table 4. The colours of the curve correspond to those of the two segments of the profile, as shown by dashed lines in map view in Fig. 20.

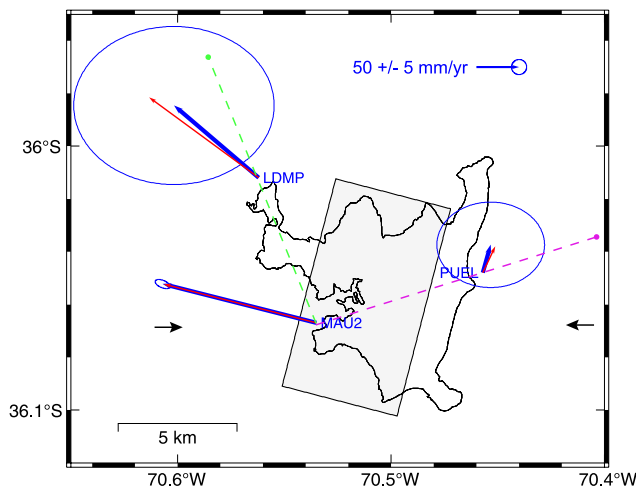


Figure 20. Map of velocity field in 2012, showing horizontal components of velocity with respect to the stable interior of South America as measured by GPS (blue arrows with 95 per cent-confidence ellipses) and velocity as modelled (red arrows) using the parameters estimated from the 2012 InSAR data, after the affine transformation described by the parameters listed in Table 4. Dashed lines indicate the profile through the deformation field shown in Fig. 19. Coordinates are latitude and longitude.

5.2 Interpretation of the modelling results

The assumption of uniform elastic properties in a half-space is a heuristic model to account for the most salient features of the observed deformation field. For example, neglecting the effect of topographic loading is justified because the estimated depth (~ 5 km) of the sill is greater than the ~ 1 km of topographic relief surrounding the LdM basin (Cayol & Cornet 1998). On the other hand, the estimated depth is likely to be deeper in a more realistic (but more computationally expensive) model with a heterogeneous distribution of material properties than in a model with a homogenous distribution (Cattin *et al.* 1999; Masterlark 2007). To mitigate this effect, we have imposed bounds of 4.7–5.3 km on the depth parameter, as noted above.

Another caveat involves the pressure within the modelled magma chamber. The model of a pressurized prolate spheroid (Yang *et al.* 1988) yields an estimate of pressure that is unrealistically large.

Indeed, the estimated annual increase in pressure exceeds the lithostatic value of 120–150 MPa expected at a depth of 5 km, assuming a density of 2500–3000 kg m⁻³ for the overburden. Although the pressurized penny-shaped crack model yields smaller, more reasonable estimates of pressure, the ratio of depth to radius is approximately ~ 1 , much less than the minimum value of 2.5 required for the calculated displacements to be accurate within 3 per cent (Sun 1969). Alternatively, one would expect a lower estimate of the pressure and better fit to the data by allowing the amount of opening on the sill to decrease with distance from its centre (Yun *et al.* 2006).

We note that the Mogi (1958) model with four adjustable parameters fits the InSAR data better than does the Yang *et al.* (1988) model with 8 adjustable parameters, as indicated by the cost values of 0.1274 and 0.1388 cycles, respectively, for the resampled pixels in the 3-yr interferogram (Fig. 7a). The volume change in the infinitesimal, spherical (Mogi) parametrization is effectively concentrated at the estimated depth, whereas half of the finite pressurized cavity in the prolate-spheroidal Yang formulation is distributed above the estimated depth. Consequently, the difference in misfit between the two corresponding solutions is likely to be a result of the 4.7-to-5.3-km constraint on the depth parameter, as discussed below.

Among the four models for the magmatic source, the Okada (1985) parametrization (tensile opening on a rectangular sill) provides the best fit to the InSAR data. The Okada model yields the lowest value of the objective function. For example, we compare the residual phase values from the Okada model to those from the Mogi model for the resampled pixels in the 3-yr interferogram (Fig. 7a). Following Feigl & Thurber (2009), we use the two-sample statistic v_2 given by Mardia & Jupp (2000) in their eq. (7.3.24). We test the null hypothesis that the von Mises concentration parameters of the phase residuals from the two models are equal $\kappa(\mathbf{m}^{\text{Okada}}) = \kappa(\mathbf{m}^{\text{Mogi}})$. The corresponding mean resultant lengths are $\bar{R}(\mathbf{m}^{\text{Okada}}) = 0.6642$ and $\bar{R}(\mathbf{m}^{\text{Mogi}}) = 0.5914$, respectively for the two sets of residual phase values. The number of data $n = 6043$ in both solutions. Since the two-sample statistic $v_2 = 8.49$ is greater than the two-tailed critical value $Z_{0.975} = 1.96$ for the standard normal distribution at the 0.05 significance level, we reject the null hypothesis. Thus the Okada residuals are more concentrated than the Mogi residuals. Therefore, we infer that the Okada model fits the InSAR data significantly better than does the Mogi model with 95 per cent confidence.

Taken together, the arguments above favour the Okada (1985) model of tensile opening on a rectangular sill below the LdM volcanic field. In summary, the Okada model: (1) is a valid approximation to the geometric configuration at LdM; (2) allows the length, width, and dip of the sill to vary to match the shape of the elongated fringe pattern observed in the InSAR data and (3) has the best fit to the InSAR data.

5.3 Implications for the eruptive cycle at LdM

The model of an inflating sill is also supported by other observations. A zone of anomalously low electrical resistivity lies at 4–5 km depth beneath the western side of the LdM rhyolite dome ring, according to a magneto-telluric (MT) data set collected by Alterra Power. The projection of the sill source estimated from the 2007–2010 InSAR data falls within a few kilometres east of the oval-shaped area of low resistance in a preliminary 2-D inversion of the MT data (Martyn Unsworth, personal communication, 2011). Our interpretation involves a fluid-rich zone associated with a magma chamber located in the upper crust beneath the region of maximum surface deformation.

The LdM area is also seismically active. An earthquake with a magnitude of 5.5 occurred on 2012 June 07 some ~ 15 km west of LdM and ~ 9 km south–southwest of Tatara-San Pedro volcano (OVDAS 2012). A preliminary analysis of 12 months of data retrieved from five local broad-band seismometers in the LdM basin in 2012 April reveals dozens of shallow earthquakes that occurred between the surface and 5 km depth in three swarms below the southern half of the postglacial rhyolite dome ring, as reported by the seismology team at OVDAS. Two types of earthquakes (short-period, volcano-tectonic earthquakes with magnitudes as large as 1.5 and long-period earthquakes) are concentrated in these zones, suggesting that magma and/or hydrothermal fluids may be accumulating in, and/or ascending from, a reservoir at a depth of ~ 5 km.

One cluster of these shallow earthquakes and the centre of the measured uplift are located within 5 km of the vent of the Rhyolite of Colada Las Nieblas (unit ‘rln’). Although this flow has not yet been dated, we infer that it is among the youngest eruptions in the volcanic field, based on its lack of pumice cover and low degree of erosion. Its proximity to the locus of unrest suggests that the inflation that began in 2007 is driven by the same large magma body that fed the postglacial silicic eruptions since ~ 25 ka.

The rate of uplift at LdM is among the highest ever observed geodetically for a volcano that is not actively erupting. To our knowledge, the rate at Campi Flegrei (Italy) is unsurpassed. During a brief episode of unrest between 1982 and 1984, the total vertical displacement accumulated was 1.8 m (Trasatti *et al.* 2011; Dvorak & Berrino 1991). The rapid deformation at LdM, however, has continued for more than 5 yr.

A similar style of deformation, albeit at much lower rates, occurred during the recent inflation episodes at three other large, silicic volcanic systems. For example, the rate of vertical uplift at LdM is larger by a factor of at least seven than that measured by GPS at Yellowstone in the United States (Chang *et al.* 2010), as shown in Fig. 21. At Santorini (Greece), the rate of inflation of 180 mm yr^{-1} measured by GPS has been attributed to a source at 4 km depth that expanded by $14 \times 10^6 \text{ m}^3$ between 2011 January and 2012 January (Newman *et al.* 2012). In the central Andes, the Lazufre volcanic area has also been actively deforming since 1998 with a maximum inflation rate of $\sim 25 \text{ mm yr}^{-1}$ (Froger *et al.* 2007). The affected area is large—roughly $\sim 50 \text{ km} \times \sim 38 \text{ km}$ (Anderssohn *et al.* 2009)—and the deformation source has been modelled as a sill at a depth between 7 and 15 km (Froger *et al.* 2007; Ruch *et al.* 2008; Anderssohn *et al.* 2009; Ruch *et al.* 2009; Ruch & Walter 2010; Budach *et al.* 2013). Its average volumetric inflation rate is ‘about $14 \times 10^6 \text{ m}^3 \text{ yr}^{-1}$ ’ (Froger *et al.* 2007).

The high rate of uplift observed at LdM is not constant. Since the rate of vertical uplift at LdM has accelerated from zero in 2003–2004 to more than 250 mm yr^{-1} in 2007–2012, the causative process must be episodic. On longer timescales, a field observation supports the inference of episodic processes. A set of dipping, (undated) lacustrine sediments are exposed only on the west side of LdM, suggesting a previous episode of unrest.

Over geological timescales, volcanic eruptions have deposited numerous lavas and tuffs in a spectacular concentric ring (Hildreth *et al.* 2010). Their similar chemical compositions represent the culmination of an eruptive sequence from andesite to dacite to rhyolite. Considering the 6.4 km^3 of postglacial rhyolite erupted in the last 19 ka as the 15-per cent residue left by fractional crystallization of a larger body of parental basalt, we estimate the rate of volume increase to be of the order of $\sim 2 \times 10^6 \text{ m}^3 \text{ yr}^{-1}$ (Andersen *et al.* 2012). Over the last 1.5 Ma, at least 350 km^3 of material has erupted at LdM, for a mean rate of $0.2 \times 10^6 \text{ m}^3 \text{ yr}^{-1}$ (Hildreth *et al.* 2010).

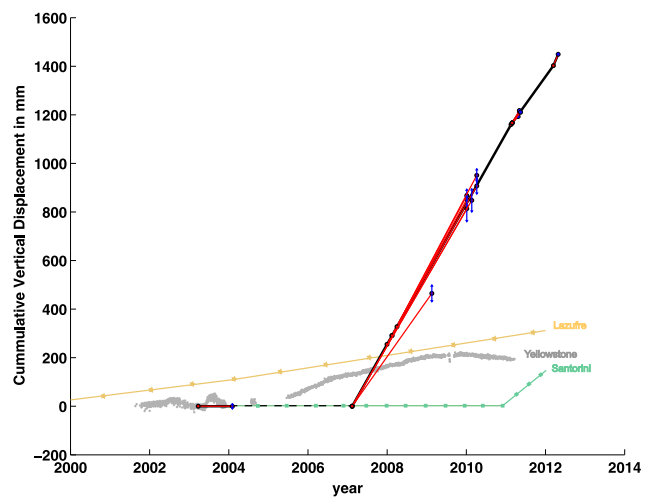


Figure 21. Time-series of vertical displacement u_z calculated as the maximum over the study area from the model parameters estimated using: ENVISAT data from 2003 to 2004 (Fournier *et al.* 2010), ALOS data from 2007 to 2010, TanDEM-X data from 2011 and TerraSAR-X data from 2012. Plotting conventions for the temporal adjustment are the same as in Fig. 18. Grey curve shows vertical uplift at Yellowstone (United States) as measured by GPS (Chang *et al.* 2010). Yellow curve (stars) shows vertical uplift at Lazufre (Chile), as inferred from InSAR (Pearse & Lundgren 2013), assuming purely vertical motion and an incidence angle of 23° from vertical. Green curve (squares) shows vertical uplift at Santorini (Greece), as measured by GPS and InSAR (Papoutsis *et al.* 2013).

This rate is of the same order of magnitude as eruptive rates averaged over intervals of $\sim 10^5$ to 10^6 yr at well-dated frontal arc complexes (Singer *et al.* 2008). Although the flux rate estimated from erupted volumes cannot be directly compared to that estimated from elastic models of deformation without accounting for the compressibility of the magma (Rivalta & Segall 2008; Johnson *et al.* 2000), the long-term rates are slower than the 5-yr rates estimated over 2007–2012 by one or two orders of magnitude. These comparisons indicate that the magmatic processes driving the deformation must be episodic. The processes driving these unrest episodes must be complex, as illustrated by the variety of eventual outcomes at other volcanoes. In the cases of Yellowstone, Santorini, and Lazufre, the unrest ended harmlessly. At Rabaul volcano in Papua New Guinea, however, an episode of unrest ended in 1984 with a ‘geodetically quiet’ 10-yr interval, after which the volcano began to erupt in 1994 (McKee *et al.* 1984; Geyer & Gottsmann 2010; Ronchin *et al.* 2013). Unlike Eliot (1925), we do not know whether the unrest at LdM will end with ‘a bang’ or ‘a whimper’.

6 CONCLUSION

The geodetic measurements indicate exceptionally rapid rates of deformation at LdM from 2007 to 2012. The rate of vertical displacement at LdM accelerated from at least 200 mm yr^{-1} in 2007 to more than 280 mm yr^{-1} in 2012, as shown in Fig. 21. The fringes from three independent InSAR data sets, including ALOS (2007–2010), Tandem-X (2011 January–March) and TerraSAR-X (2012 March–April) show a consistent spatial pattern. The large signal also appears in GPS measurements at three continuously operating stations. It cannot be explained by artefacts related to the effects of tropospheric gradients, ionospheric disturbances, orbital errors or topographic relief. We reject the hypothesis that changes in the

level of water impounded behind the dam cause the deformation by gravitational loading and unloading.

We therefore attribute the deformation at LdM to inflation of a sill at depth of 4.7–5.3 km. Assuming a dislocation in a half-space composed of a uniform, Poisson elastic solid, we estimate the length of the sill to be 6–9 km and its width to be 5–6 km. Within the modelled sill, the maximum rate of inflation of $51 \pm 8 \times 10^6 \text{ m}^3 \text{ yr}^{-1}$ (i.e. $1.6 \pm 0.3 \text{ m}^3 \text{ s}^{-1}$) occurred in early 2012. During the 5.3-yr interval from 2007 January to 2012 April, the volume of the modelled sill increased by at least 0.15 cubic kilometres. The change in volume could be the result of magma migration or injection. It could also be the result of increasing pressure of volatile phases exsolving from hot magma.

These results lead to the hypothesis that the rhyolite vents have tapped a ~20-km-diameter layer of melt that extends under the entire basin at LdM (Hildreth *et al.* 2010). Accordingly, the current episode of unrest indicates the continuing growth of a large silicic system by incremental emplacement of sills (e.g. Annen 2009; Petford *et al.* 2000). Testing this hypothesis and evaluating the hazard associated with the ongoing unrest will require a multidisciplinary study, including mineralogical, petrological, seismological, magneto-telluric and gravimetric measurements. Careful numerical modelling of such measurements will enhance understanding of the underlying processes over timescales ranging from days ($\sim 10^4$ s) to millions of years ($\sim 10^{13}$ s).

ACKNOWLEDGEMENTS

We gratefully express *muchas gracias* to Luis Torres Jara, the volunteer *Alcalde de Mar*, for assistance, information, and hospitality at LdM. We thank Christophe Vigny and Jaime Campos of the International (Chilean/French) Laboratory ‘Montessus de Ballore’ for sharing GPS data from 2012 from the station at MAUL. We also thank Carlos Cardona, Matt Pritchard, Jeremy Pesicek and Cliff Thurber for helpful discussions. Careful criticism from two anonymous reviewers improved the manuscript. Several figures were created using the Generic Mapping Tools—GMT (Wessel & Smith 1998). We gratefully acknowledge support from the Weeks family to the Department of Geoscience at the University of Wisconsin-Madison. SAR data from the TerraSAR-X (Pitz & Miller 2010) and the TanDEM-X (Krieger *et al.* 2007) satellite missions operated by the German Space Agency (DLR) were used under the terms and conditions of Research Project RES1236. PALSAR data from the ALOS satellite mission (Rosenqvist *et al.* 2007) operated by the Japanese Space Agency (JAXA) were used under the terms and conditions of the third Research Announcement (Project 93). HLM, NLA and STA were partially supported by a grant from the Graduate School at UW-Madison. Research was partially supported by a grant from the U.S. National Science Foundation (EAR-0810134) and the National Aeronautics and Space Administration (NASA-NNX12AO37G).

REFERENCES

Ali, S.T. & Feigl, K.L., 2012. A new strategy for estimating geophysical parameters from InSAR data: application to the Krafla central volcano, Iceland, *Geochem. Geophys. Geosyst.*, **13**, doi:10.1029/2012GC004112.
 Andersen, N.L., Singer, B.S., Jicha, B.R., Hildreth, E.W., Fierstein, J. & Rogers, N.W., 2012. Evolution of rhyolite at Laguna del Maule, a rapidly inflating volcanic field in the Southern Andes, in *Proceedings of the Fall Meeting of Am Geophys. Un.*, San Francisco.

Anderssohn, J., Motagh, M., Walter, T.R., Rosenau, M., Kaufmann, H. & Oncken, O., 2009. Surface deformation time series and source modeling for a volcanic complex system based on satellite wide swath and image mode interferometry: the Lazufre system, central Andes, *Rem. Sens. Environ.*, **113**, 2062–2075.
 Annen, C., 2009. From plutons to magma chambers: thermal constraints on the accumulation of eruptible silicic magma in the upper crust, *Earth planet. Sci. Lett.*, **284**, 409–416.
 Arnaud, A., Adam, N., Hanssen, R., Inglada, J., Duro, J., Closa, J. & Eineder, M., 2003. ASAR ERS interferometric phase continuity, *IEEE Int. Geosci. Rem. Sens. Symp.*, **2**, 1133–1135.
 Bähr, H. & Hanssen, R.F., 2012. Reliable estimation of orbit errors in spaceborne SAR interferometry, *J. Geod.*, **86**, 1147–1164.
 Beauducel, F., Briole, P. & Froger, J.L., 2000. Volcano wide fringes in ERS synthetic aperture radar interferograms of Etna: deformation or tropospheric effect?, *J. geophys. Res.*, **105**, 16 391–16 402.
 Biggs, J., Wright, T., Lu, Z. & Parsons, B., 2007. Multi-interferogram method for measuring interseismic deformation: Denali Fault, Alaska, *Geophys. J. Int.*, **170**, 1165–1179.
 Brocher, T.M., 2005. Empirical relations between elastic wavespeeds and density in the Earth’s crust, *Bull. seism. Soc. Am.*, **95**, 2081–2092.
 Budach, I., Brasse, H. & Díaz, D., 2013. Crustal-scale electrical conductivity anomaly beneath inflating Lazufre volcanic complex, Central Andes, *J. S. Am. Earth Sci.*, **42**, 144–149.
 Cattin, R., Briole, P., Lyon-Caen, H., Bernard, P. & Pinettes, P., 1999. Effects of superficial layers on coseismic displacements for a dip-slip fault and geophysical implications, *Geophys. J. Int.*, **137**, 149–158.
 Cayol, V. & Cornet, F.H., 1998. Effects of topography on the interpretation of the deformation field of prominent volcanoes: application to Etna, *Geophys. Res. Lett.*, **25**, 1979–1982.
 Chang, W.-L., Smith, R.B., Farrell, J. & Puskas, C.M., 2010. An extraordinary episode of Yellowstone caldera uplift, 2004–2010, from GPS and InSAR observations, *Geophys. Res. Lett.*, **37**, L23302, doi:10.1029/2010GL045451.
 CNES, 2006. *DIAPASON Automated Interferometric Processing Software*, Centre National d’Etudes Spatiales.
 DeMets, C., Gordon, R.G. & Argus, D.F., 2010. Geologically current plate motions, *Geophys. J. Int.*, **181**, 1–80.
 Dvorak, J.J. & Berrino, G., 1991. Recent ground movement and seismic activity in Campi Flegrei, southern Italy: episodic growth of a resurgent dome, *J. geophys. Res.: Solid Earth*, **96**, 2309–2323.
 Eliot, T.S., 1925. The Hollow Men, in *Poems, 1909–1925*, Faber & Gwyer, pp. 98.
 Falorni, G., Teles, V., Vivoni, E.R., Bras, R.L. & Amaratunga, K.S., 2005. Analysis and characterization of the vertical accuracy of digital elevation models from the Shuttle Radar Topography Mission, *J. geophys. Res.*, **110**, doi:10.1029/2003JF000113.
 Feigl, K.L. & Thurber, C.H., 2009. A method for modelling radar interferograms without phase unwrapping: application to the M 5 Fawnskin, California earthquake of 1992 December 4, *Geophys. J. Int.*, **176**, 491–504.
 Feigl, K.L., Gasperi, J., Sigmundsson, F. & Rigo, A., 2000. Crustal deformation near Hengill volcano, Iceland 1993–1998: coupling between volcanism and faulting inferred from elastic modeling of satellite radar interferograms, *J. geophys. Res.*, **105**(26), 555–525, 670.
 Fialko, Y. & Simons, M., 2000. Deformation and seismicity in the Coso geothermal area, Inyo County, California: observations and modeling using satellite radar interferometry, *J. geophys. Res.*, **105**, 21 781–21 794.
 Fialko, Y., Khazan, Y. & Simons, M., 2001. Deformation due to a pressurized horizontal circular crack in an elastic half-space, with applications to volcano geodesy, *Geophys. J. Int.*, **146**, 181–190.
 Fournier, T.J., Pritchard, M.E. & Riddick, S.N., 2010. Duration, magnitude, and frequency of subaerial volcano deformation events: new results from Latin America using InSAR and a global synthesis, *Geochem. Geophys. Geosyst.*, **11**, Q01003, doi:10.1029/2009GC002558.
 Froger, J.L., Remy, D., Bonvalot, S. & Legrand, D., 2007. Two scales of inflation at Lastarria-Cordon del Azufre volcanic complex, central Andes,

- revealed from ASAR-ENVISAT interferometric data, *Earth planet. Sci. Lett.*, **255**, 148–163.
- Geyer, A. & Gottsmann, J., 2010. The influence of mechanical stiffness on caldera deformation and implications for the 1971–1984 Rabaul uplift (Papua New Guinea), *Tectonophysics*, **483**, 399–412.
- Goldstein, R.M. & Werner, C.L., 1998. Radar interferogram filtering for geophysical applications, *Geophys. Res. Lett.*, **25**, 4035–4038.
- Grandin, R. et al., 2009. September 2005 Manda Hararo–Dabbahu rifting event, Afar (Ethiopia): constraints provided by geodetic data, *J. geophys. Res.*, **114**, B08404, doi:10.1029/2008JB005843.
- Hanssen, R.F., 2001. *Radar Interferometry: Data Interpretation and Error Analysis*, Kluwer, pp. 328.
- Harris, J.M., Hirst, J.L. & Mossinghoff, M.J., 2008. *Combinatorics and Graph Theory*, 2nd edn, Vol. xv, Springer, p. 381.
- Hildreth, W., Godoy, E., Fierstein, J. & Singer, B., 2010. Laguna del Maule Volcanic field: eruptive history of a Quaternary basalt-to-rhyolite distributed volcanic field on the Andean range crest in central Chile, *Servicio Nacional de Geología y Minería – Chile, Boletín*, **63**, 142 pp.
- Johnson, D.J., Sigmundsson, F. & Delaney, P.T., 2000. Comment on “Volume of magma accumulation or withdrawal estimated from surface uplift or subsidence, with application to the 1960 collapse of Kilauea volcano” by P. T. Delaney and D. F. McTigue, *Bull. Volcanol.*, **61**, 491–493.
- Jonsson, S., Zebker, H., Segall, P. & Amelung, F., 2002. Fault slip distribution of the 1999 Mw 7.1 Hector Mine, California, Earthquake, estimated from satellite radar and GPS measurements, *Bull. seism. Soc. Am.*, **92**, 1377–1389.
- Kohlhase, A.O., Feigl, K.L. & Massonnet, D., 2003. Applying differential InSAR to orbital dynamics: a new approach for estimating ERS trajectories, *J. Geod.*, **77**, 493–502.
- Krieger, G., Moreira, A., Fiedler, H., Hajnsek, I., Werner, M., Younis, M. & Zink, M., 2007. TanDEM-X: a Satellite Formation for High-Resolution SAR Interferometry, *IEEE Trans. Geosci. Rem. Sens.*, **45**, 3317–3341.
- Lohman, R.B. & Simons, M., 2005. Some thoughts on the use of InSAR data to constrain models of surface deformation: noise structure and data downsampling, *Geochem. Geophys. Geosyst.*, **6**, 01007, doi:10.1029/2004GC000841.
- Lorito, S. et al., 2011. Limited overlap between the seismic gap and coseismic slip of the great 2010 Chile earthquake, *Nat. Geosci.*, **4**, 173–177.
- Mardia, K.V., 1972. *Statistics of Directional Data*, Academic Press, pp. 357.
- Mardia, K.V. & Jupp, P.E., 2000. *Directional Statistics*, 2nd edn, pp. 429, Wiley.
- Massonnet, D. & Feigl, K.L., 1995. Discriminating geophysical phenomena in satellite radar interferograms, *Geophys. Res. Lett.*, **22**, 1537–1540.
- Massonnet, D. & Feigl, K.L., 1998. Radar interferometry and its application to changes in the Earth’s surface, *Rev. Geophys.*, **36**, 441–500.
- Massonnet, D. & Rabaute, T., 1993. Radar interferometry: limits and potential, *IEEE Trans. Geosci. Rem. Sens.*, **31**, 455–464.
- Massonnet, D., Rossi, M., Carmona, C., Adragna, F., Peltzer, G., Feigl, K. & Rabaute, T., 1993. The displacement field of the Landers earthquake mapped by radar interferometry, *Nature*, **364**, 138–142.
- Massonnet, D., Feigl, K.L., Rossi, M. & Adragna, F., 1994. Radar interferometric mapping of deformation in the year after the Landers earthquake, *Nature*, **369**, 227–230.
- Masterlark, T., 2007. Magma intrusion and deformation predictions: sensitivities to the Mogi assumptions, *J. geophys. Res.: Solid Earth*, **112**, B06419, doi:10.1029/2006JB004860.
- McKee, C.O., Lowenstein, P.L., Saint Ours, P., Talai, B., Itikarai, I. & Mori, J.J., 1984. Seismic and ground deformation crises at Rabaul Caldera: prelude to an eruption?, *Bull. Volcanol.*, **47**, 397–411.
- McLeod, I.H., Cumming, I.G. & Seymour, M.S., 1998. ENVISAT ASAR data reduction—impact on SAR interferometry, *IEEE Trans. Geosci. Rem. Sens.*, **36**, 589–602.
- Mogi, K., 1958. Relations between the eruption of various volcanoes and the deformations of the ground surfaces around them, *Bull. Earthq. Res. Inst.*, **36**, 99–134.
- Newman, A.V. et al., 2012. Recent geodetic unrest at Santorini Caldera, Greece, *Geophys. Res. Lett.*, **39**, L06309, doi:10.1029/2012GL051286.
- Nikolaïdis, N. & Pitas, I., 1998. Nonlinear processing and analysis of angular signals, *IEEE Trans. Signal Proc.*, **46**, 3181–3194.
- Nof, R.N., Ziv, A., Doin, M.P., Baer, G., Fialko, Y., Wdowinski, S., Eyal, Y. & Bock, Y., 2012. Rising of the lowest place on Earth due to Dead Sea water-level drop: evidence from SAR interferometry and GPS, *J. geophys. Res.: Solid Earth*, **117**, B05412, doi:10.1029/2011jb008961.
- Okada, Y., 1985. Surface deformation due to shear and tensile faults in a half-space, *Bull. seism. Soc. Am.*, **75**, 1135–1154.
- OVDAS, 2012. *Earthquake Report, Observatorio Volcanológico de los Andes del Sur (OVDAS), Servicio Nacional de Geología y Minería (SERNA-GEOMIN)*, Temuco, Chile.
- Papoutsis, I., Papanikolaou, X., Floyd, M., Ji, K.H., Kontoes, C., Paradissis, D. & Zacharis, V., 2013. Mapping inflation at Santorini volcano, Greece, using GPS and InSAR, *Geophys. Res. Lett.*, **40**, 267–272.
- Pearse, J. & Lundgren, P., 2013. Source model of deformation at Lazufre volcanic center, central Andes, constrained by InSAR time series, *Geophys. Res. Lett.*, **40**, 1059–1064.
- Petford, N., Cruden, A.R., McCaffrey, K.J.W. & Vigneresse, J.L., 2000. Granite magma formation, transport and emplacement in the Earth’s crust, *Nature*, **408**, 669–673.
- Pinel, V. & Jaupart, C., 2000. The effect of edifice load on magma ascent beneath a volcano, *Phil. Trans. R. Soc. Lond. Ser. A: Math., Phys. Eng. Sci.*, **358**, 1515–1532.
- Pinel, V., Sigmundsson, F., Sturkell, E., Geirsson, H., Einarsson, P., Gudmundsson, M.T. & Arnadóttir, T., 2007. Discriminating volcano deformation due to magma movements and variable surface loads: application to Katla subglacial volcano, Iceland, *Geophys. J. Int.*, **169**, 325–338.
- Pitz, W. & Miller, D., 2010. The TerraSAR-X Satellite, *IEEE Trans. Geosci. Rem. Sens.*, **48**, 615–622.
- Rivalta, E. & Segall, P., 2008. Magma compressibility and the missing source for some dike intrusions, *Geophys. Res. Lett.*, **35**, L04306, doi:10.1029/2007GL032521.
- Ronchin, E., Masterlark, T., Molist, J.M., Saunders, S. & Tao, W., 2013. Solid modeling techniques to build 3D finite element models of volcanic systems: an example from the Rabaul Caldera system, Papua New Guinea, *Comput. Geosci.*, **52**, 325–333.
- Rosenqvist, A., Shimada, M., Ito, N. & Watanabe, M., 2007. ALOS PAL-SAR: a pathfinder mission for global-scale monitoring of the environment, *IEEE Trans. Geosci. Rem. Sens.*, **45**, 3307–3316.
- Ruch, J., Anderssohn, J., Walter, T.R. & Motagh, M., 2008. Caldera-scale inflation of the Lazufre volcanic area, South America: evidence from InSAR, *J. Volc. Geotherm. Res.*, **174**, 337–344.
- Ruch, J., Manconi, A., Zeni, G., Soloro, G., Pepe, A., Shirzaei, M., Walter, T.R. & Lanari, R., 2009. Stress transfer in the Lazufre volcanic area, central Andes, *Geophys. Res. Lett.*, **36**, L22303, doi:10.1029/2009GL041276.
- Ruch, J. & Walter, T.R., 2010. Relationship between the InSAR-measured uplift, the structural framework, and the present-day stress field at Lazufre volcanic area, central Andes, *Tectonophysics*, **492**, 133–140.
- Samet, H., 1984. The quadtree and related hierarchical data structures, *ACM Comput. Surv.*, **16**, 187–260.
- Schmidt, D. & Burgmann, R., 2003. Time-dependent land uplift and subsidence in the Santa Clara valley, California, from a large interferometric synthetic aperture radar data set, *J. geophys. Res.*, **108**, doi:10.1029/2002JB002267.
- Segall, P., 2010. *Earthquake and Volcano Deformation*, pp. 432, Princeton Univ. Press.
- Simons, M., Fialko, Y. & Rivera, L., 2002. Coseismic deformation from the 1999 Mw 7.1 Hector Mine, California, earthquake as inferred from InSAR and GPS observations, *Bull. seism. Soc. Am.*, **92**, 1390–1402.
- Singer, B., Hildreth, W. & Vincze, Y., 2000. 40Ar/39Ar evidence for early deglaciation of the central Chilean Andes, *Geophys. Res. Lett.*, **27**, 1663–1666.
- Singer, B.S., Jicha, B.R., Harper, M.A., Naranjo, J.A., Lara, L.E. & Moreno-Roa, H., 2008. Eruptive history, geochronology, and magmatic evolution of the Puyehue-Cordon Caulle volcanic complex, Chile, *Bull. geol. Soc. Am.*, **120**, 599–618.
- Snyder, J.P., 1982. *Map Projections used by the U.S. Geological Survey*, 2nd edn, Vol. 1532, pp. 313, U.S. Gov’t Print. Off.

- Sun, R.J., 1969. Theoretical size of hydraulically induced horizontal fractures and corresponding surface uplift in an idealized medium, *J. geophys. Res.*, **74**, 5995–6011.
- Trasatti, E., Bonafede, M., Ferrari, C., Giunchi, C. & Berrino, G., 2011. On deformation sources in volcanic areas: modeling the Campi Flegrei (Italy) 1982–84 unrest, *Earth planet. Sci. Lett.*, **306**, 175–185.
- Turcotte, D.L. & Schubert, G., 2002. *Geodynamics*, 2nd edn, pp. 456, Cambridge University Press.
- Vigny, C. *et al.*, 2011. The 2010 Mw 8.8 Maule Megathrust Earthquake of Central Chile, monitored by GPS, *Science*, **332**, 1417–1421.
- Wessel, P. & Smith, W.H.F., 1998. New, improved version of generic mapping tools released, *EOS, Trans. Am. geophys. Un.*, **79**, 459.
- Yang, X.-M., Davis, P.M. & Dieterich, J.H., 1988. Deformation from inflation of a dipping finite prolate spheroid in an elastic half-space as a model for volcanic stressing, *J. geophys. Res.*, **93**, 4249–4257.
- Yun, S., Segall, P. & Zebker, H., 2006. Constraints on magma chamber geometry at Sierra Negra Volcano, Galápagos Islands, based on InSAR observations, *J. Volc. geotherm. Res.*, **150**, 232–243.
- Zumberge, J.F., Heflin, M.B., Jefferson, D.C., Watkins, M.M. & Webb, F.H., 1997. Precise point positioning for the efficient and robust analysis of GPS data from large networks, *J. geophys. Res.*, **102**, 5005–5017.